Simulating Contrails and Their Impact on Incoming Solar Radiation at the Surface on the Regional Scale - A Case Study

Numerische Simulationen von Kondensstreifen und deren Auswirkung auf die empfangene solare Einstrahlung an der Erdoberfläche auf der regionalen Skala - Eine exemplarische Untersuchung

Master Thesis in Meteorology

Simon Gruber

Oktober 2015

INSTITUTE OF METEOROLOGY AND CLIMATE RESEARCH
KARLSRUHE INSTITUT OF TECHNOLOGIE (KIT)

Adviser:	Prof. Dr. Christoph Kottmeier
Second Adviser:	Prof. Dr. Corinna Hoose

Zusammenfassung

Kondensstreifen gehören zu den am deutlichsten sichtbaren Zeichen für den Einfluss anthropogener Aktivität auf die Atmosphäre.

Um dieses Phänomen zu simulieren, wurde das hoch auflösende regionale Atmosphärenmodell COSMO-ART (Baldauf et al., 2011; Vogel et al., 2009) um eine Parametrisierung erweitert, welche es erlaubt, die Entstehung sowie den Lebenszyklus von Kondensstreifen zu berechnen.

Basierend auf dem Schmidt-Appleman-Kriterium (Schumann, 1996) berechnet die Parametrisierung den Quellterm für Kondensstreifeneis. Der nun folgende Lebenszyklus, welcher unter anderem Prozesse wie Advektion, Wasserdampfdeposition, Sublimation und Kollisionsprozesse beinhaltet, wird durch ein Zwei-Momenten-Wolkenmikrophysikschema (Seifert and Beheng, 2006) beschrieben. Dieses wurde durch Einführung einer eigenen Eisklasse für Kondensstreifeneis erweitert. Mit dem so erweiterten Modellsystem ist es möglich, sogenannte Kondensstreifenzirren, die aus gealterten Kondensstreifen bestehen und deren Lebenszyklus zu simulieren. Kondensstreifenzirren können sich in räumlich ausgedehnte, optisch dünne Zirren entwickeln.

Die zusätzlich entstehenden Zirren modifizieren den Strahlunsghaushalt der Atmosphäre. Um diesen Effekt zu quantifizieren, wurde das Strahlungsschema derart angepasst, dass es den Anforderungen der sehr kleinen Eispartikeln in Kondensstreifen gerecht wird. In dieser Konfiguration ist die vorliegende Arbeit unserer Kenntnis nach die erste hochaufgelöste regionale Modellstudie für Kondensstreifen.

Der zugrunde liegende, einzigartige Datensatz für den Flugverkehr wurde vom Institut für Flugverkehr und Flughafenforschung (DLR, Köln) zur Verfügung gestellt. Er enthält für ein begrenztes Gebiet über Mitteleuropa zeitlich und räumlich hoch aufgelöste Flugzeugtrajektorien, welche aus Echtzeitdaten abgeleitet wurden.

Mit dem so erweiterten Modellsystem wurde eine Fallstudie durchgeführt, bei der über Deutschland mit Ausnahme von natürlichen Zirren und Kondensstreifen keine anderen Wolkentypen vorlagen. Es zeigt sich, dass die Berücksichtigung von Kondensstreifen und vor allem von Kondensstreifenzirren im Modell die Satellitenbeobachtung deutlich besser nachbildet. Neben den Bedingungen für die Kondensstreifenbildung werden ebenfalls die mikrophysikalischen Eigenschaften über den kompletten Lebenszyklus von Kondensstreifen und Kondensstreifenzirren sowie deren Einfluss auf die natürliche Zirrusbewölkung über Mitteleuropa untersucht. Sowohl junge als auch gealterte Kondensstreifen unterscheiden sich hinsichtlich der hohen Partikelanzahldichte und der kleinen mittleren Kristallradien signifikant von natürlichen Zirren. Es wird gezeigt, dass sich zum einen der Bedeckungsgrad in den höheren Atmosphärenschichten durch zusätzliches Kondensstreifeneis erhöht, zum anderen nimmt die Bedeckung von natürlichen Zirren aufgrund der Bil-

dung von Kondensstreifen ab. Ehemals für Zirren verfügbarer Wasserdampf ist nun in Kondensstreifen und deren weiteren Entwicklungsstufen gespeichert.

Da Kondensstreifen auch strahlungswirksam sind, wird ihr Einfluss auf den Strahlungshaushalt und die Modifikation des Strahlungsbudgets an der Erdoberfläche auf der regionalen Skala quantifiziert. Neben einem leicht positiven Beitrag im thermischen Bereich überwiegt die Abschattung und damit eine Reduzierung der am Erdboden ankommenden kurzwelligen Strahlung. Obwohl diese Effekte durch eine Verdrängung von natürlichen Wolken teilweise kompensiert werden, bleibt ein negativer Nettobeitrag von bis zu $10\ \%$ Prozent.

Contents

1. Introduction

Anthropogenic activities influence the processes of the earth's atmosphere in various ways. Of special importance are the emissions of trace gases and aerosols that directly and indirectly modify the radiation budget of our planet. An important part of meteorological research consists of the quantification of these impacts and the estimation of the future evolution.

Besides the modification of profiles for radiative active gases like carbon dioxide and nitric oxides by direct emissions, air traffic especially causes changes by contrails and the indirect aerosol effect. The latter two phenomena are not well understood till now, but nevertheless quite easily to observe. They occur mostly in the upper troposphere and lower stratosphere. In both areas processes take place that are of a certain importance for the radiative budget of the atmosphere, as they offer favorable conditions for cirrus clouds.

The indirect aerosol effect describes changes of microphysical properties as well as changes in the frequency of occurrence and the extent of coverage for natural clouds due to the emission of aerosol particles (Hendricks et al., 2005). By entraining environmental air, ice particles form in the exhaust plume of aircrafts. This phenomenon is called contrail. Contrails only occur with special environmental conditions, that are described in the Schmidt-Appleman-Theory (Schmidt, 1941; Appleman, 1953; Schumann, 1996). With a favorable state of the atmosphere, characterized by very low temperatures and strong supersaturation with respect to ice, the originally line shaped contrails undergo various physical processes on the micro scale, spread by influence of shear and advection and change as well in their structure as also in their microphysical properties until they are not to be distinguished from natural cirrus. This type of artificial cloud is called contrail cirrus, describing cirrus-like clouds developing from contrails (Heymsfield et al., 2010). For very favorable conditions, they survive for several hours. The overall change in natural cloudiness raised by line shaped contrails as well as contrail cirrus is termed as aircraft induced cloudiness (Heymsfield et al., 2010).

Contrails, contrail cirrus and contrail induced cloudiness in general influence the radiative budged in a way that is comparable to thin natural cirrus clouds (Sausen et al., 2005). Important properties like the optical depth or the spatial and temporal extent of occurrence are still not investigated well enough and also not quantified to a satisfying extent (Forster et al., 2007). One assumes that the influence of aged contrails and contrail induced cirrus is of a stronger importance that the one

originating from young, line shaped contrails (Stubenrauch et al., 2005; Eleftheratos et al., 2007).

Different methods exist to measure both properties and spreading of contrails and contrail cirrus. First attempts tried estimating the coverage with line shaped contrails over certain areas by visually analyzing satellite images (Bakan et al., 1994). In further steps, detection algorithms (Mannstein et al., 1999) were developed for investigating coverage, microphysical and optical properties of contrails, but still with the major drawback, that these methods require line shaped contrails. Aged and spreaded contrails as well as contrail cirrus cannot be detected. A promising attempt is the development of a tracking algorithm (Vázquez-Navarro et al., 2012) that allows besides determining the optical depth of contrail cirrus also investigating larger parts of contrail life cycle.

Former model studies mainly used global circulation models extended by parameterizations that are able to simulate line shaped and aged contrails (Ponater et al., 1996, 2002, 2005; Marquart et al., 2003; Burkhardt et al., 2011). The global influence on radiation can be examined, although averaging in time and area is required. In this context, a global mean of contrail coverage of 0.1 to 2 % seems to be neglectable (Myhre, 2013). But still, there are estimations for situations with up to 10% for example over Central Europe (Burkhardt et al., 2011). Compared to a globally mean radiative forcing of about 6 to 15 $mW\ m^{-2}$, local impacts of more than 300 $mW\ m^{-2}$ are possible (Burkhardt et al., 2011). Major drawbacks of this approach are a certain vagueness in terms of spatial and temporal resolution of the short-lived and small-scaled phenomenon and the simplified treatment of microphysical processes.

Another group of projects approaches single contrails with large-eddy-models (Unterstrasser, 2014; Lewellen et al., 2001). Here, the evolution of ice particels in the exhaust plume and the fluid dynamics of wake vortex formation and decay are represented in detail. Parameter studies allow investigating the conditions under which contrails are persistent and the manner, microphysical and optical properties change during the transition into wide spread contrail cirrus and their final decay. An obvious drawback of this method is the not existent possibility to apply such a model on a larger ensemble of contrails with a not-prescribed meteorological situation. To quantify the impact of air traffic on the state of the atmosphere, it is therefore not suitable.

The presented study combines both approaches and is, to our knowledge, the first one of its kind. The regional atmospheric model COSMO-ART (Baldauf et al., 2011; Vogel et al., 2009) is used. It allows besides a high spatial and temporal resolution also the treatment of processes that deal with the influence of aerosols and trace gases. The model is extended by a parameterization based on recent results from large-eddy-simulations (Unterstrasser, 2014; Schumann, 2012) for taking into account the formation of contrails. Although using to a certain extent the method of the Contrail Cirrus Prediction Tool (Schumann, 1996) for the calculation of initial values, the further stages of contrail life cycle follow a different approach. As ice crystals in young contrails are much smaller than the ones forming natural cirrus clouds and occur in much higher number density (Schröder

et al., 2000; Voigt et al., 2010; Febvre et al., 2009), the microphyics scheme needs certain modifications to satisfy the special requirements of young contrail ice particles. Obviously, a simple bulk microphysics scheme treating ice only with respect to its mass is not able to represent the characteristics of contrails and contrail cirrus. Therefore, the operational cloud microphyics routines are replaced by a more sophisticated scheme that uses a two moment approach (Seifert and Beheng, 2006). The latter is extended by a new hydrometeor class allowing a separate treatment of the small contrail ice crystals apart from natural ice. This approach allows investigating contrail microphsical properties and their changes during the various stages of development represented in a regional atmospheric model.

Concerning the contrail microphysics as well as the interaction with the meteorological situation, the whole procedure presented so far is online coupled, avoiding a diagonstic treatment of contrails in contrast to other models on a comparable grid scale (Schumann, 2012). One of the key goals of this project is therefore the quantification of the influence of contrails and contrail cirrus on natural high level cloudiness.

Besides the contrail microphysics, also and especially the radiative properties and their local influence on short wave radiation budget at the surface are investigated. The model uses a diagnostic radiation scheme (Fu et al., 1998). The parameterization of the shortwave optical properties for ice clouds is optimized for different naturally occuring particle habits (Key et al., 2002). This is why the parameterization needs to be modificated for not falling short in describing the optical properties of the crystals with very small diameters present in young contrails. The presented method serves to study the impact of contrails, contrail cirrus and contrail induced cloudiness on the radiative budget at the surface on a regional scale and short time spans comparable to weather forecast modeling. This gains certain importance in line of predicting the energy yield from photovoltaic systems.

Another feature of this work is the new and recently developed data set that lies beyond. Instead of statistical calculations for globally averaged fuel consumption (Ferrone, 2011), the basic data consists of exact flight trajectories over a limited area, that are recorded from real time based data (flightradar24, 2015) and provided by the Institute of Air Transport and Airport Research, DLR, Cologne, Germany.

2. Model Description

This chapter is dedicated to the basic equations and parameterizations used in this thesis. First, a short overview over the regional atmospheric model COSMO-ART, which serves as a frame work, is presented. Then, the routines to calculate the microphysical properties of ice particles and the modifications to represent contrails as well as the applied radiation scheme are described.

2.1 COSMO-ART

This study is based on the model system COSMO-ART, that will be briefly described in this chapter. COSMO stands for Consortium for Small Scale Modeling and gives name to the numerical weather prediction model, developed by the German Weather Service (DWD). In operational service since 1999 and developed from the former Lokal-Modell (LM), for the higher resolved DE domain, mainly covering Central Europe, COSMO is still in charge, whereas for the larger EU domain, the ICON model (Zängl et al., 2015) is already established. It is also still in use with various other weather services and especially when it comes to atmospheric research purposes, COSMO often is the tool of first resort.

COSMO is a non-hydrostatic model, solving the primitive thermodynamic equations of a moist atmosphere assuming an incompressible fluid. A more detailed description of the basic equations and their numerical implementation can be found in Baldauf et al. (2011). Still they are mentioned here for the sake of completeness. In their following form, they are already Reynolds-averaged. The corresponding abbreviations are listed in Tab. 2.1.

$$\rho\frac{d\vec{v}}{dt} = -\nabla p + \rho\vec{g} - 2\vec{\Omega}\times(\rho(\vec{v})) - \nabla\cdot\mathbb{T} \tag{2.1}$$

$$\frac{dp}{dt} = -\frac{c_p}{c_v}p\nabla\cdot\vec{v} + \left(\frac{c_p}{c_v} - 1\right)Q_h \tag{2.2}$$

$$\rho c_p\frac{dT}{dt} = \frac{dp}{dt} + Q_h \tag{2.3}$$

$$\rho\frac{dq_v}{dt} = -\nabla\vec{F}_v - (I_l + I_i) \tag{2.4}$$

$$\rho \frac{dq_{l,i}}{dt} = -\nabla \cdot (\vec{P}_{l,i} + \vec{F}_{l,i}) + I_{l,i} \tag{2.5}$$

$$\rho = p \left[R_d \left(1 + \left(\frac{R_v}{R_d} - 1 \right) q_v - q_l - q_i \right) T \right]^{-1} \tag{2.6}$$

The indices stand for:

d	dry air
i	ice
l	liquid water
v	water vapor

Table 2.1: Abbreviations used in Eqs. 2.1 - 2.6.

ρ	density	Q_h	diabatical heating / cooling
$\vec{\Omega}$	angular speed of Earth's rotation	q_x	specific mass mixing ratio
$\vec{F}_x$	turbulent flux	R_x	specific gas constant
$\vec{g}$	gravitational acceleration	t	time
I_x	sources / sinks (phase transitions)	$\mathbb{T}$	Reynolds Stress tensor
p	pressure	$\vec{v}$	wind velocity
$\vec{P}_x$	precipitation		

Equations 2.1 to 2.6 are transformed into a rotating coordinate system. Next, horizontal homogeneous stationary and hydrostatic basic state is introduced by splitting each variable into a basic value and its derivation. Applying this method causes horizontal pressure gradients in the basic state to vanish. This minimizes numerical errors for pressure when assuming only small derivations from the reference state. These modifications yield a set of prognostic differential equations that are being solved, using the method of finite differences.

As the regional model is not capable of covering the whole globe, boundary as well as initial data needs to be prescribed. This is done, using the relaxation method after Davies at the boundaries, whereas Rayleigh damping is applied at the vertical end of the model domain. Various sources for data are available. In operational service, a data assimilation chain is used, whereas in general, boundary conditions are provided by a model with a coarser resolution.

The ART extension (Vogel et al., 2009), with ART representing Aerosol and Reactive Trace Gases was developed at the Institute for Meteorology and Climate Research (IMK) at the Karlsruhe Institute for Technology (KIT). It provides a tool to calculate various processes involving aerosol and gas phase chemistry as well as the diffusion of these species. An outstanding feature of the model system is the modular and completely online coupled structure. Both variables characterizing the state of the atmosphere and such for describing chemistry are calculated within one single simulation. A diagnostic way of treatment does not allow feedback mechanisms comparable to COSMO-ART (Fig. 2.1).

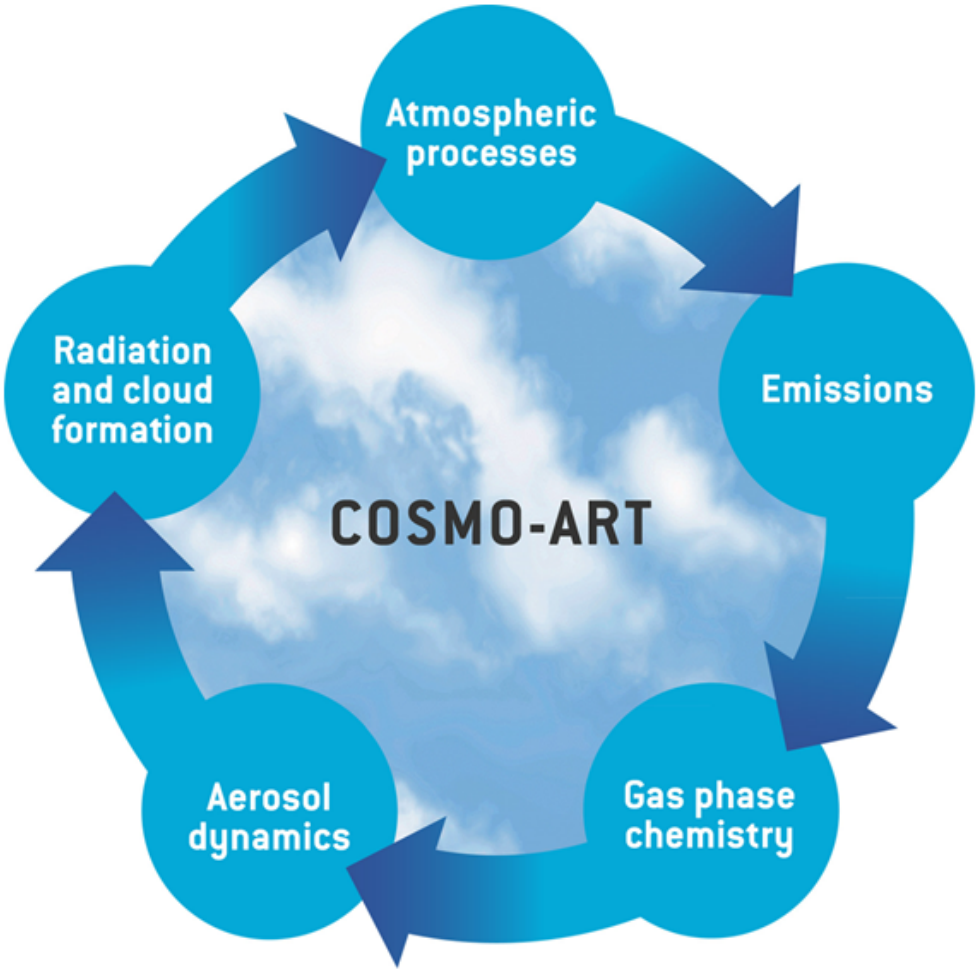

Figure 2.1: Schema of the model system COSMO-ART (Vogel et al., 2009).

2.2 The Two-Moment Cloud Microphysics Scheme

Since each single cloud is a very complex, non linear system that interacts in various ways with the embedding atmosphere, modeling clouds is a demanding task. Compromises have to be found between a detailed and precise, but time consuming treatment using spectral budget equations and a less exact but more efficient parameterization that calculates several integral size distributions.

To deal with scientific issues, the COSMO model may be coupled with a more sophisticated scheme for treating the cloud microphysics, than the operational bulk scheme. The scheme that uses a two moment approach (Seifert and Beheng, 2006) actually represents the basic framework of this study.

Up till now, only one class describing ice particles occuring in high level ice clouds was available and optimized for crystals in natural cirrus. To satisfy the demandings that go along with the simulation of contrail ice particles, that is in first place the small initial diameters and their large number concentration, a separate class was introduced. Besides the microphysical properties concerning the geometry and ventilation of these crystals, also the basic microphysical processes in young contrails need to be treated carefully and separately from the natural cirrus ice.

The following chapter first contains a short introduction to the basic equations of the two moment scheme after Seifert and Beheng (2006). Second, the applied modifications for an accurate treatment of contrails are described.

2.2.1 Overview

Generally, the scheme calculates both mass and number densities of six different hydrometeor types, including cloud droplets, rain drops, cloud ice, snow, graupel and hail. These classes are separated from each other by virtue of their different shapes and sizes as well as in the microphysical processes they experience. Especially the specific shape and mean particle mass is decisively influencing the effectiveness of various processes as these quantities determine additionally both the settling velocity and the mean particle surface area.

Basic cloud properties may be described as the partial power moments M_k^n of the number density size distribution of a species $f_k(x)$. The latter depends on the mass x of a single particle. The n^th moment satisfies:

$$M_k^n = \int_0^\infty x^n f_k(x) dx \tag{2.7}$$

The first two moments of $f_k(x)$ represent the number density $M_k^0 = N_k$ and the mass density $M_k^1 = M_k$ of the hydrometeor species k. Size distributions of each hydrometeor type are approx-

imated according to a generalized $\Gamma-$distribution with four coefficients A, ν, λ and μ.

$$f(x) = Ax^{\nu} \exp\left(-\lambda x^{\mu}\right) \tag{2.8}$$

The parameters A and λ, respectively, follow from the number N and mass density L.

$$A = \frac{\mu N}{\Gamma\left(\frac{\nu+1}{\mu}\right)} \lambda^{\frac{\nu+1}{\mu}} \tag{2.9}$$

$$\lambda = \left[\frac{\Gamma\left(\frac{\nu+1}{\mu}\right)}{\Gamma(\frac{\nu+2}{\mu})} \overline{x}\right]^{-\mu} \tag{2.10}$$

In Eq. 2.10, $\overline{x} = L/N$ denotes the mean particle mass. Applying these relations, the $\Gamma-$distribution can be expressed depending on number and mass densities:

$$f(x) = \frac{N}{\overline{x}} \left[\frac{x}{\overline{x}}\right]^{\nu} \frac{\mu}{\Gamma\left(\frac{\nu+1}{\mu}\right)} \left[\frac{\Gamma\left(\frac{\nu+2}{\mu}\right)}{\Gamma\left(\frac{\nu+1}{\mu}\right)}\right]^{\nu+1} \exp\left(-\left[\frac{\Gamma\left(\frac{\nu+2}{\mu}\right)}{\Gamma\left(\frac{\nu+1}{\mu}\right)} \frac{x}{\overline{x}}\right]^{\mu}\right) \tag{2.11}$$

This yield the moment to the power of n:

$$M^n = \frac{\Gamma\left(\frac{n+\nu+1}{\mu}\right)}{\Gamma\left(\frac{\nu+1}{\mu}\right)} \left[\frac{\Gamma\left(\frac{\nu+1}{\mu}\right)}{\Gamma\left(\frac{\nu+2}{\mu}\right)}\right]^{n} N\overline{x}^n \tag{2.12}$$

Like the rest of the model, also the microphysical scheme basically solves budget equations for each moment. In Cartesian coordinates, the budget for the n^{th} moment reads as:

$$\frac{\partial M_k^n}{\partial t} + \nabla \cdot \left[\vec{v} M_k^n\right] - \nabla \left[K_h \nabla M_k^n\right] + \frac{\partial}{\partial z}\left[\overline{v}_{sed,k} M_k^n\right] = S_k^n \tag{2.13}$$

Here, K_h is the turbulent diffusivity of heat, $\vec{v}$ stands for the mean wind velocity, $\overline{v}_{sed,k}$ for the mean sedimentation velocity of species k. The term $-\nabla[K_h \nabla M_k^n]$ parameterizes the turbulent fluxes. All of the sources and sink processes like nucleation, condensation, evaporation, collision, coalescence and breakup are contained in S_k^n. For the contrail ice particles, nucleation is not calculated in line of the microphysics routines but instead within its own parameterization, that is described in chapter 3, representing the only source term.

2.2.2 The Treatment of Contrail Ice

A first attempt with simply providing young contrails as source term for cloud ice and looking at the difference to a reference run turned out to strongly overestimate the amount of the effect, as only cirrus ice with a large particle number density was produced. This approach neglects the decisive differences between ice crystals occurring in aircraft exhaust plumes and particles existing

in natural cirrus, since the formation of contrails follows different physical processes compared to natural ice clouds.

Cirrus generally are found in a highly ice supersaturated environment when a slight ascending vertical movement is present. Based on the high supersaturation and a low concentration of ice nuclei available, mostly heterogeneous nucleation takes place, resulting in few but large ice crystals. In contrast, contrail ice arises from homogeneous nucleation, the particles are about one order of magnitude smaller than natural cirrus crystals. Additionally, number concentrations up to $150\ cm^{-3}$ can be observed in a young contrail. Also, measurement indicate, that freshly formed ice crystals in a contrail are best described with hexagonal columns instead of the usual mixture of shapes for cirrus ice. This underlines in the importance of assuming different coefficients for geometry and ventilation, resulting in different sedimentation velocities. Besides, also the calculation of the effective radii for contrail ice particles strongly hinges on these values.

To better represent these special properties of young contrails, their microphysical processes are treated separately from the natural cloud ice, but nevertheless allowing the possibility for the different classes for cloud ice and contrails to interact on each other. This procedure helps studying the life cycle of young contrails as well as their influence on natural cirrus. As still the contrails microphysics is embedded in the cloud scheme, a diagnostic treatment of the relevant processes can be avoided.

In the following, the most important microphysical parameterizations and their modifications for treating contrail ice are described.

Simplifications and Assumptions

Microphysical processes observed in the atmosphere usually hinge on the shape and geometry of the assumed crystal type. Basically, each single ice particle is of a unique kind, mostly influenced by its origin and possibly behaving completely different compared to others at the same surrounding macrophysical conditions. To assure efficient computing of the relevant processes in numerical model, a reduction of the complexity in terms of geometry is important. When classifying the various hydrometeor species, assumptions are made concerning their characteristics, particularly their shape or behavior while being sedimented, respectively. Additionally, those properties are averaged per mean particle mass.

One of the key figures for microphysics is the ventilation coefficient $F_{ven}(x)$, usually approximated by Eq. 2.14, with the kinematic viscosity of air ν_{air}, the Schmidt number $N_{Sc} = 0.71$, and the Reynolds number N_{Re}. The latter follows from Eq. 2.15.

$$F_{ven} = a_{ven} + b_{ven} N_{Sc}^{1/3} N_{Re}^{1/2} \tag{2.14}$$

$$N_{Re}(x) = \frac{v(x)D(x)}{\nu_{air}} \tag{2.15}$$

Both, the particle diameter D and the mean sedimentation velocity v are calculated using power laws (Eq. 2.22 and Eq. 2.28). To simplify various equations, the coefficients a_{ven} and a_{ven} for the n^{th} moment are averaged by:

$$\overline{a}_{ven,n} = a_{ven} \frac{\Gamma\left(\frac{\nu_a+n+b_{geo}}{\mu_a}\right)}{\Gamma\left(\frac{\nu_a+1}{\mu_a}\right)} \left[\frac{\Gamma\left(\frac{\nu_a+1}{\mu_a}\right)}{\Gamma\left(\frac{\nu_a+2}{\mu_a}\right)}\right]^{b_{geo}+n-1} \tag{2.16}$$

$$\overline{b}_{ven,n} = b_{ven} \frac{\Gamma\left(\frac{\nu_a+n+\frac{3}{2}b_{geo}+\frac{1}{2}b_{vel}}{\mu_a}\right)}{\Gamma\left(\frac{\nu_a+1}{\mu_a}\right)} \left[\frac{\Gamma\left(\frac{\nu_a+1}{\mu_a}\right)}{\Gamma\left(\frac{\nu_a+2}{\mu_a}\right)}\right]^{\frac{3}{2}b_{geo}+\frac{1}{2}b_{vel}+n-1} \tag{2.17}$$

These relations follow from the integration of the general $\Gamma-$distribution (Eqs. 2.18 and 2.19). Finally, a_{ven} and b_{ven} for particles are hold constant, obtained values of these as well as assumptions for b_{ven} and b_{vel} are found in Tab. 2.2.

$$f_a(x) = Ax^{\nu_a} exp\left(-\lambda x^{\mu_a}\right) \tag{2.18}$$

$$\int_0^\infty D(x) F_{ven}(x) f(x) x^{n-1} dx = N D(\overline{x}) \overline{x}^{n-1} \overline{F}_{ven,n}(\overline{x}) \tag{2.19}$$

This yields the following formulations for the ventilation coefficient for water vapor and heat, respectively:

$$\overline{F}_{ven,1} = \overline{a}_{ven,1} + \overline{b}_{ven,1} N_{Sc}^{1/3} N_{Re}^{1/2}(\overline{x}_i) \tag{2.20}$$

$$F_h = \frac{D_T}{D_v} F_{ven} = \frac{K_T}{c_p \rho_0 D_v} F_{ven} \tag{2.21}$$

Here, D_T and D_v are the diffusivity of heat and water vapor, respectively, K_T stands for the conductivity of heat and c_p denotes the specific heat capacity of air.

Another basic quantity in cloud microphysics is the mean particle diameter D in dependence on the mean particle mass, taking into account the shape of the particles. In general, the diameter-mass relation (Eq. 2.22) is approximated by a power law, with specific coefficients a_{geo} and b_{geo}. The relation between the mean mass of a particle ensemble and the mean diameter using Eq. 2.22 is depicted in Fig. 2.2. The mean diameter of the smallest particles taken into account is about $1.2\ \mu m$ and comprises basically the recently formed particles in a young contrail. Particles, that

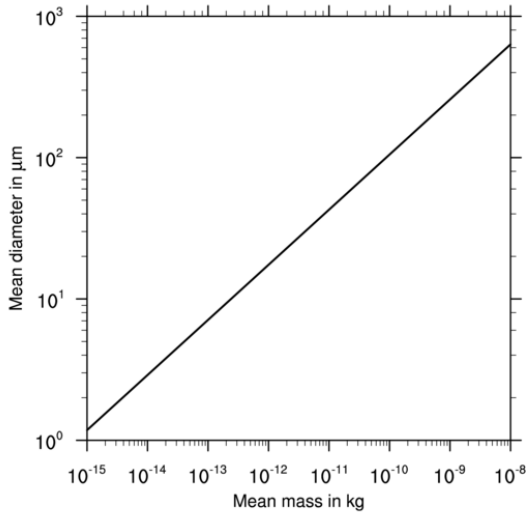

Figure 2.2: Mean diameter of contrail ice particles depending on mean mass.

reach sizes over about $600\ \mu m$ are considered to behave in a similar way like natural ice and are not treated in separately from the latter anymore.

$$D(x) \approx a_{geo} x^{b_{geo}} \tag{2.22}$$

The applied microphysical constants as well as the coefficients for the assumed $\Gamma-$distribution for contrail and contrail cirrus ice, respectively are listed in Tab. 2.2. Parameters for the $\Gamma-$distribution are the same for every class of ice hydrometeors and therefore remain unchanged for contrails, indicating that the same shape of the curve is assumed, only shifted to much smaller masses.

Determining the shape of ice crystals in young contrails is a difficult task, as the minimum threshold for detection of instruments usually is too high to capture correctly the very small particles (Febvre et al., 2009). These particles are classified as 'unresolved spherical' (Lawson et al., 1998). Here, about $99\ \%$ of a particle ensemble in a young contrail has diameters smaller than $20\ \mu m$ and is assumed to be a assortment of plates, columns and other spheroid structures, the small fraction of crystals between 100 and $250\ \mu m$ forms bullet rosettes.

Since no single particles are traced in the model, the individual shapes cannot be regarded in detail but need to be averaged. Straightforward, the geometrical factors a_{geo} and b_{geo} are taken from (Gierens et al., 1997), describing the contrail ice crystals as small hexagonal columns. This method obtains similar growth rates compared to large-eddy-simulations (Lewellen et al., 2001). The coefficients a_{vel} and b_{vel} are used to calculate the sedimentation velocity (Eq. 2.28). The resulting sedimentation velocities presented above agree with a parameterization for the general

Table 2.2: Microphysical constants of contrail ice particles.

Symbol	Definition	Value	Unit	Reference
x_{max}	maximum particle mass	10^{-8}	kg	Unterstrasser (2008)
x_{min}	minimum particle mass	10^{-15}	kg	Unterstrasser (2008)
ν	constant in size distribution	0.0	$-$	Seifert and Beheng (2006)
μ	constant in size distribution	0.333	$-$	Seifert and Beheng (2006)
a_{geo}	constant in diameter-mass-relation	11.0	$m^{-1}\ kg^{-b_{geo}}$	Gierens et al. (1997)
b_{geo}	constant in diameter-mass-relation	0.45	$-$	Gierens et al. (1997)
a_{ven}	constant in ventilation coefficient	0.780	$-$	Hall and Pruppacher (1976)
b_{ven}	constant in ventilation coefficient	0.308	$-$	Hall and Pruppacher (1976)
a_{vel}	constant in fallspeed relation	$6.66 \cdot 10^5$	$m\ s^{-1}\ kg^{-b_{vel}}$	Böhm (1989)
b_{vel}	constant in fallspeed relation	0.667	$-$	Böhm (1989)

equation for the terminal fall speed of solid hydrometeors (Böhm, 1989) for the limit of small spheroid particles. Finally the coefficients for ventilation a_{ven} and b_{ven} remain the same like the ones used for cloud ice (Seifert and Beheng, 2006).

Depositional Growth and Sublimation

As mentioned above, pristine ice crystals in a recently formed contrail have small diameters. The corresponding sedimentation velocities are too slow to allow this process a notable role in the early stage of contrail microphysics. The same is true for all kinds of collection processes. Nevertheless they represent an effective sink in the aged stage of contrail life time, but in the early phase, the mass of a contrail crystal ensemble that is comparable to values in cirrus clouds, usually is distributed over a huge number of particles. In addition, a larger crystal falling through the population is not able to collect the tiny particles, as they are ventilated around the collector crystal.

By virtue of this, the substantive source term in the early stage of the contrail life is growth because of deposition of water vapor in case of supersaturation. In fact, this process depends on size, shape and ventilation of the particles as well as on supersaturation with respect to ice and several other meteorological parameters. The major process causing crystal loss is sublimation in a subsaturated environment. To parameterize the depositional growth and sublimation of ice particles, respectively, a general growth equation (Pruppacher and Klett, 1997) is applied.

$$\left.\frac{dx}{dt}\right|_{dep} = \frac{4\pi C F_{ven}\left(x\right) S_i}{\frac{R_v T}{e_{sat,i}(T) D_v} + \frac{L_{iv}}{K_T T}\left(\frac{L_{iv}}{R_v T} - 1\right)} = \frac{4\pi}{C} D G_{iv}\left(T, p\right) F_{ven}\left(x\right) S_i \tag{2.23}$$

with

$$G_{iv}\left(T, p\right) = \left[\frac{R_v T}{e_{sat,i} D_v} + \frac{L_{iv}}{K_T T}\left(\frac{L_{iv}}{R_v T} - 1\right)\right]^{-1} \tag{2.24}$$

Here, T is the temperature, $C \approx D/\pi$ denotes the capacity of hexagonal particles. S_i is the supersaturation with respect to ice, L_{iv} stands for the latent heat of sublimation, $e_{sat,i}$ denotes the saturation vapor pressure over and R_v names the specific gas constant for water vapor.

To calculate the temporal derivative of the mass density (IWC) of a particle ensemble, Eq. 2.23 is integrated:

$$\left.\frac{\partial IWC}{\partial t}\right|_{dep} = \int_0^\infty \left.\frac{dx}{dt}\right|_{dep} f(x)dx = \frac{4\pi}{C} G_{iv}(T,p) S_i \int_0^\infty D(x) F_{ven}(x) f(x) dx \tag{2.25}$$

Finally, applying the $\Gamma-$distribution results in an relation that now depends on the mean mass of a particle ensemble ($\overline{x}$):

$$\left.\frac{\partial IWC}{\partial t}\right|_{dep} = \frac{4\pi}{C} D\left(\overline{x}\right) G_{iv}\left(T, p\right) \overline{F}_{ven} S_i \tag{2.26}$$

In case of subsaturation, ice particles start to sublimate. As this process follows the same physical laws like the depositional growth, this parameterization computes both, sublimation and deposition.

The ratio of deposed or sublimated mass and particle mean mass per time step relative to relative humidity with respect to ice is shown in Fig. 2.3. For sensivity studies, the ice water content was held on a constant value of $IWC = 0.1\ mg\ m^{-3}$, while the mean mass is varying between $10^{-15}\ kg$ and $10^{-8}\ kg$ indicated by different colors, see Tab. 2.3, resulting in particle number densities of $10^8\ m^{-3}$ to $10\ m^{-3}$. This covers the spread of common values occurring in both young contrails and thin cirrus clouds (Schröder et al., 2000). In case of supersaturation, a surplus environmental water vapor may diffuse towards the crystals surfaces, increasing their mass and diameter. As the total surface of an ensemble consisting of many small particles is larger than in the case of few but larger individuals, depositional growth is most effective for the smallest ensemble. Also an exponential increase with supersaturation is observed.

If the surrounding air is subsaturated with respect to ice, the crystals sublimate, indicated by a loss of mass and number density, respectively. For better comparison, the sublimated mass in Fig. 2.3 is taken as absolute value. This process is very effective with the smaller crystals, for example,

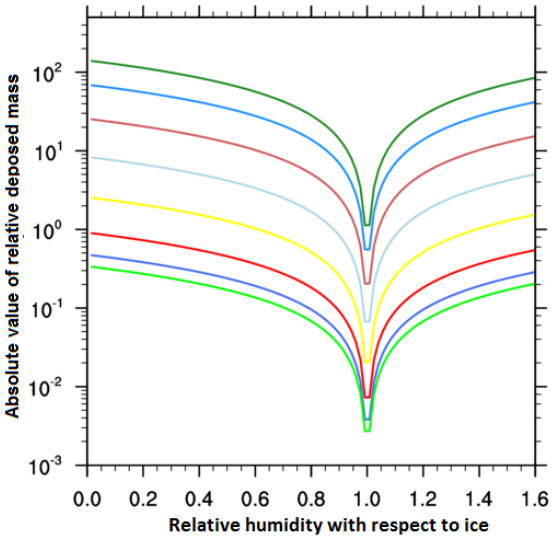

Figure 2.3: Absolutle value of relative particle growth due to deposition / sublimation per model time step depending on ambient humidity for different mean crystal masses, $IWC = 1.0\ 10^{-7}\ kg\ m^{-3}$, $\Delta t = 25\ s$ (details see text).

Table 2.3: Assumed properties of the crystal ensembles in Fig. 2.3 and Fig. 2.4.

color	D in μm	N in m^{-3}	x in kg
dark green	1.2	10^8	10^{-15}
dark blue	2.9	10^7	10^{-14}
dark red	7.1	10^6	10^{-13}
light blue	17.4	10^5	10^{-12}
yellow	42.8	10^4	10^{-11}
red	105.1	10^3	10^{-10}
blue	258.0	10^2	10^{-9}
green	633.4	10^1	10^{-8}

in case of $RH_i < 0.9$, ensembles with mean diameters up to 7.1 μm sublimate within one time step ($\Delta t = 25\ s$). Larger particles survive a far lower subsaturation.

As a two moment scheme is applied here, besides the mass, also the number density of a particle ensemble has to be considered. Additionally, microphysical processes and the radiative impact of ice crystals are very sensitive to the mean diameter that is implicitly described by the mass to number ratio. Therefore it is crucial, especially with the present high amount of individuals in a young contrail, to consider the decrease of particle numbers in case of sublimation.

The number of particles remains constant in case of depositional growth. In contrast, for $\left.\frac{\partial IWC}{\partial t}\right|_{dep} < 0$, a weighting factor f_n (Eq. 2.27) is applied to estimate the loss in number density.

$$f_n = \left(\frac{IWC\,(t) - IWC\,(t - \Delta t)}{IWC\,(t)} \bigg|_{dep} \right)^{\alpha} \tag{2.27}$$

The relation in brackets in Eq. 2.27 describes the ratio of mass being lost within one time step. It turned out, that the exponent α is to be varied between 1.0 and 1.5 (Harrington et al., 1995). In this study, corresponding to Unterstrasser (2008), $\alpha = 1.1$ is used. Fig. 2.4 displays the surviving fraction in terms of mass and number densities with respect to subsaturation. The colors indicate the same ensembles like in Fig. 2.3, solid lines represent the surviving mass ratio, the dashed lines the surviving number ratio, respectively.

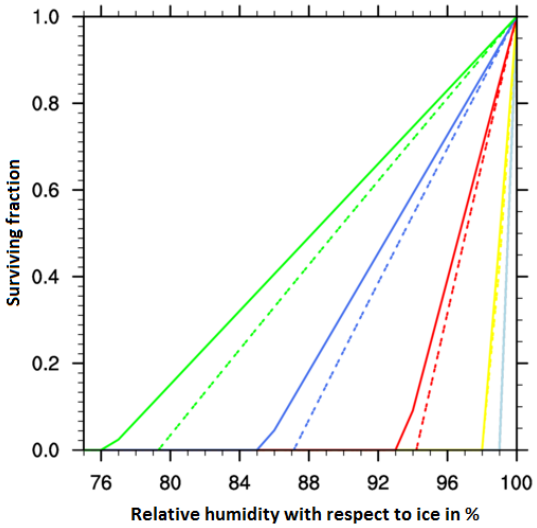

Figure 2.4: Surviving fraction of mass and number density in case of sublimation for different mean crystal masses per model time step, $IWC = 1.0\ 10^{-7}\ kg\ m^{-3} = const., \Delta t = 25\ s$ (details see text).

As α is chosen $<\ 1$, it is assured, that a larger fraction of mass than of numbers is lost. The parameterization of sublimation therefore forces the mean diameter of an ensemble to decrease.

2.3 Sedimentation

Sedimentation is the loss of hydrometeors on the basis of their gravitational acceleration in direction of the earth's surface. For contrails and contrail cirrus, the parameterized sedimentation is similar to the one for natural ice.

Like the diameter-mass-relation, also the terminal settling velocity v is approximated by a power law with coefficients a_{vel} and b_{vel}, listed in Tab. 2.2.

$$v(x) \approx a_{vel} x^{b_{vel}} \left(\frac{\rho_0}{\rho}\right)^{1/2} \tag{2.28}$$

Assuming the generalized $\Gamma-$distribution and integrating yields a mass weighted mean fall velocity for the moment with $k = 1$:

$$\overline{v}(\overline{x}) = a_{vel} \frac{\Gamma\left(\frac{k+\nu+b_{vel}+1}{\mu}\right)}{\Gamma\left(\frac{k+\nu+1}{\mu}\right)} \left[\frac{\Gamma\left(\frac{\nu+1}{\mu}\right)}{\Gamma\left(\frac{\nu+2}{\mu}\right)}\right]^{b_{vel}} \overline{x}^{b_{vel}} \tag{2.29}$$

The same fraction of both mass and number of particles being lost in virtue of sedimentation is

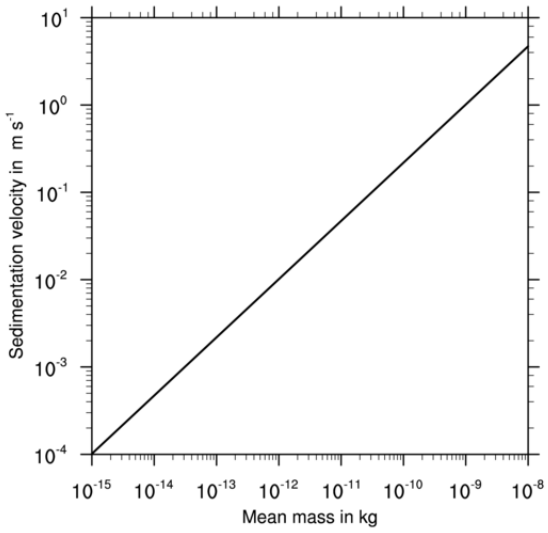

Figure 2.5: Sedimentation velocity of contrail ice particles depending on mean mass.

determined by the calculated sedimentation velocity. Values of the sedimentation velocity for the implemented contrail ice class are displayed in Fig. 2.5. Crystals in a young contrail are remarkably small and light, their settling velocity therefore is rather small, too. But nevertheless, the aged particles may reach fall speeds larger than $1\ m\ s^{-1}$, allowing sedimentation to be an effective sink.

Collection Processes

Another important phenomenon in cloud microphysics is the collection of ice and coagulation of warm phase particles respectively. Following Seifert and Beheng (2006), instead of pre-calculated collection integrals stored in a lookup table, a different approach, making use of a mean collision efficiency E and a collection kernel K_{ab} to approximate the interaction of particle ensembles is applied.

As no decisive modifications have been done here to treat contrails and the contrail ice class requires mainly depends on a parameterized selfcollection, only the basic idea behind the theory is presented. A detailed description can be found in Seifert and Beheng (2006). When both the mean particle radius and the mass density exceed a certain threshold, selfcollection is an effective process to shift the size distribution to a larger mean and reduce the overall particle number density.

The routine assumes a particle ensemble of species b is collected by an ensemble of species a, enlarging only a.

$$\left.\frac{\partial M_a^k}{\partial t}\right|_{coll,ab} = \int_0^\infty \int_0^\infty f_a(x) f_b(y) K_{ab}(x,y) \left[(x+y)^k - y^k\right] dxdy \tag{2.30}$$

$$\left.\frac{\partial M_b^k}{\partial t}\right|_{coll,ab} = -\int_0^\infty \int_0^\infty f_a(x) f_b(y) K_{ab}(x,y) y^k dxdy \tag{2.31}$$

Where K_{ab} symbolizes a kernel defined as:

$$K_{ab}(x,y) = \frac{\pi}{4} \left[D_a(x) + D_b(y)\right]^2 |v_a(x) - v_b(y)| E_{ab}(x,y) \tag{2.32}$$

For the size distributions f_a and f_b, the corresponding $\Gamma-$function is applied.

Melting

Melting is parameterized by calculating characteristic time scales τ_{melt}. The following equation (Pruppacher and Klett, 1997) describes melting of ice particles. Although contrails usually occur in regions with temperatures far below the freezing point, still advection may transport ice particles originating from aircraft induced water vapor into regions with higher temperatures. In the following equations, e_v denotes the partial pressure of water vapor with respect to ice, $e_{sat,i}$ is the saturation vapor pressure with respect to ice. The latent heat of melting is termed as L_{iv} and the abbreviation T_3 symbolizes the freezing point ($T = 273.15\ K$).

$$\frac{dx}{dt} = -\frac{2\pi}{L_{il}} D \left[K_T (T - T_3) F_h + \frac{D_v L_{iw}}{R_v} \left(\frac{e_v}{T} - \frac{e_{sat,i}(T_3)}{T_3}\right) F_{ven}\right] \tag{2.33}$$

$$\tau_{melt} = \frac{x}{\frac{dx}{dt}|_{melt}} = \frac{L_{il}}{2\pi} \frac{x}{DF_v} \left[\frac{K_T D_T}{D_v} (T - T_3) + \frac{D_v L_{iv}}{R_v} \left(\frac{e_v}{T} - \frac{e_{sat,i}(T_3)}{T_3}\right)\right]^{-1} \tag{2.34}$$

Applying this, the temporal change of the moments satisfies:

$$\begin{aligned} \left.\frac{\partial M^n}{\partial t}\right|_{melt} &= -\int_0^\infty \frac{x^n f(x)}{\tau_{melt}} dx \\ &= -\frac{2\pi}{L_{il}} \left[\frac{K_T D_T}{D_v} (T - T_3) + \frac{D_v L_{iv}}{R_v} \left(\frac{p_v}{T} - \frac{e_{sat,i}(T_3)}{T_3}\right)\right] \times \\ &\int_0^\infty D(x) F_v(x) f(x) x^{n-1} dx \end{aligned} \tag{2.35}$$

Again, assuming the generalized $\Gamma-$function yields:

$$\left.\frac{\partial M^n}{\partial t}\right|_{melt} = -\int_0^\infty \frac{x^n f(x)}{\tau_{melt}} dx$$

$$= -\frac{2\pi}{L_{il}}\left[\frac{K_T D_T}{D_v}\left(T - T_3\right) + \frac{D_v L_{iv}}{R_v}\left(\frac{e_v}{T} - \frac{e_{sat,i}\left(T_3\right)}{T_3}\right)\right] \times \tag{2.36}$$

$$ND\left(\overline{x}\right)\overline{F}_{ven}\left(\overline{x}\right)\overline{x}^{n-1} dx$$

Nucleation

Nucleation processes in contrails are not explicitly treated here. The initial mass and number densities of contrail ice are provided in a separate parameterization combining both the Schmidt-Appleman-Ciriterion and the wake vortex processes (see section 3). But nevertheless, these calculations assume homogeneous nucleation to take place in a young contrail. In a further step of this project, besides water vapor, also aerosol and trace gases are to be emitted, allowing to investigate the impact of aircraft emissions on cloud formation. But as up till now, no data is available and therefore no results to be shown, a description of the secondary nucleation processes is not presented here.

2.4 The Radiation Scheme

One of the key issues of this work is to investigate the changes in the radiative budget of atmosphere by virtue of contrails and contrail cirrus. Of special interest here is the impact on short wave radiation, as this quantity is determinative to estimate the amount of produced solar energy from photovoltaic systems.

The atmospheric radiation fluxes in the COSMO model are calculated diagnostically by the GRAALS radiation scheme (Ritter and Geleyn, 1992). For eight spectral bands, the radiative transfer equations are solved using a two-stream approximation. The radiative properties of ice clouds are computed using a one dimensional radiation scheme (Fu et al., 1998; Key et al., 2002). It separates the solar spectrum into six bands, the thermal spectrum is treated in 12 different bands, each comprising a certain realm of wave lengths. As it was optimized with respect to ice crystal ensembles, that have been measured in cirrus clouds, the scheme computes reliable values for effective radii (r_e) between 6 and 80 μm (Fu et al., 1998), whereas for particles smaller than 6 μm, the parameterization is not well defined. Unfortunately, crystals in young contrails often may have smaller effective radii, this is a problem to deal with.

For maintain a proper stability of the radiative properties of contrails, those small values for r_e are simply enlarged to 4 μm, since sensitivity studies showed that this is the decisive threshold

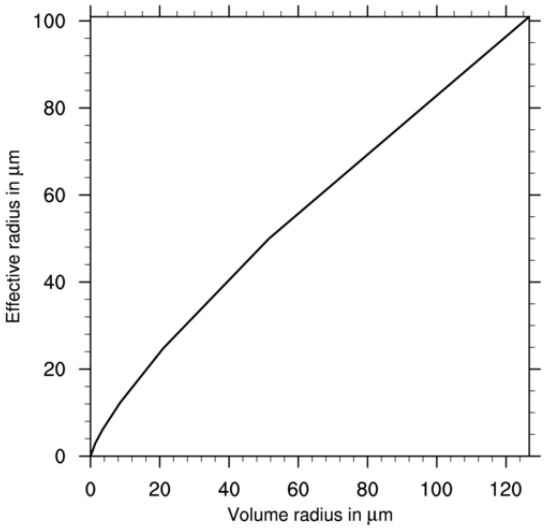

Figure 2.6: Effective radii for contrail ice particles depending on volume radius.

beneath which serious convergence problems arise. Modification of the radiation scheme is not to be done offhand and therefore remains to a further development. To estimate the arising error, a comparison was carried out. In one simulation r_e was set to zero for $r_e < 4\ \mu m$, in another, the original IWC was passed to the radiation scheme, but enlarging r_e to $4\ \mu m$ in the critical grid cells. Since no large differences occurred comparing the two simulations and furthermore, a vital impact on the radiative budget usually is meaningful only over a longer time period and contrail particles grow constantly, this simplification seems justifiable. Nevertheless one needs to keep in mind, that the routine in this configuration may underestimate the radiative effect of very young contrails.

The calculation of the contrail effective radii follows Fu et al. (1998). Here, the crystals are assumed to be hexagonal columns with their c-axes oriented parallel to the direction of light.

$$r_e = \frac{1}{2}\left(\int_{L_{min}}^{L_{max}} D^2 L n\left(L\right) dL\right)\left(\int_{L_{min}}^{L_{max}} \left(DL + \frac{\sqrt{3}}{4}D^2\right) n\left(L\right) dL\right)^{-1} \tag{2.37}$$

D denotes the width of a crystal, the length is L. For the number size distribution $n(L)$ the same generalized $\Gamma-$distribution as defined in the microphysics scheme is used. It has to be noted, that instead of a monodisperse size distribution that lays beyond the calculations for cloud ice a polydisperse size distribution is assumed for contrails, to better catch the bottom end of the length scale:

$$N\left(D\right) = N_0 D^{\nu} exp\left(-\lambda D^{\mu}\right) \tag{2.38}$$

The effective radius for different particle diameters, calculated with Eq. 2.37, is displayed in Fig.

2.6. For comparison, the mean geometrical radius after Eq. 2.22 lies beyond. As the radiation parameterization is not defined for very small values of r_e, values smaller than 3 μm are not considered.

The components of the radiative transfer equation are defined below. β in Eq. 2.39 is the extinction coefficient, $\widetilde{\omega}$ in Eq. 2.40 denotes the single scattering albedo, the asymmetry factor is abbreviated as g (Eq. 2.41) and finally, the forward scattering peak fraction is f in Eq. 2.42. The relations are computed, using fit coefficients derived from measurement in cirrus clouds (Fu et al., 1998). Details as well as the corresponding relations applied in the parameterization can be found in Appendix B.

$$\beta = IWC\left(a_0 + \frac{a_1}{2r_e} + \frac{a_2}{(2r_e)^2}\right) \tag{2.39}$$

$$\widetilde{\omega} = 1 - \left(b_0 + b_1 2r_e + b_2\left(2r_e\right)^2 + b_3\left(2r_e\right)^3\right) \tag{2.40}$$

$$g = c_0 + c_1 2r_e + c_2\left(2r_e\right)^2 + c_3\left(2r_e\right)^3 \tag{2.41}$$

$$f_\delta = d_0 + d_1 2r_e + d_2\left(2r_e\right)^2 + d_3\left(2r_e\right)^3 \tag{2.42}$$

$$f = \frac{1}{2\widetilde{\omega}} + f_\delta \tag{2.43}$$

The forward scattering fraction (Eq. 2.43) consists of a term, describing the fraction of diffracted rays, that is basically the forward scattering peak of the phase function, followed by a second term, taking the contribution from the $\delta-$function transmission through parallel plane at the zero-scattering angel into account.

Values for β are mainly depending on the effective radius. During this study, various numerical experiments were made in order to compute the extinction without overestimating the effect due to the small particle sizes. In the solar spectrum reaching from 250 nm to 3500 nm, the following relation can be applied (Ebert and Curry, 1992):

$$\beta = IWC\left(a_{SW}\right) + \frac{b_{SW}}{r_e}; \quad a_{SW} = 3.448\ m^2\ kg^{-1},\ b_{SW} = 2.431 \cdot 10^{-3}\ m^3\ kg^{-1} \tag{2.44}$$

In the CoCiP model (Schumann, 1996), the extinction is computed with:

$$\beta = IWC\frac{a_{SW}}{r_e}; \quad a_{SW} = \frac{1.5}{\rho_i} \tag{2.45}$$

For a better overview, in Fig. 2.7 the mean mass as an equivalent depending variable was chosen. The colors indicate in red Eq. 2.39, green for Eq. 2.44 and blue for Eq. 2.45, respectively.

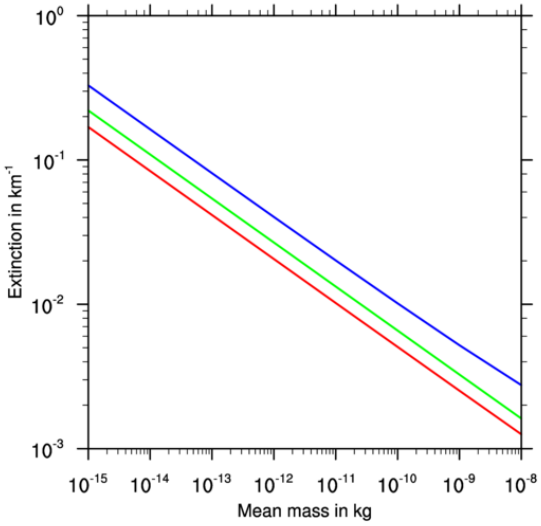

Figure 2.7: Extinction over mean mass, red: Fu et al. (1998), green: Ebert and Curry (1992) and blue: Schumann (1996).

A strong increase of the extinction with decreasing particle mass can be seen in all cases. The method after Schumann (1996) is derived for bullet-formed crystals, whereas the microphysics and the calculation of the effective radius assume columns with a hexagonal cross section. Also, Eq. 2.45) seems to constantly overestimate the effect by $\sim$ 30 % compared to the other approaches. For reasons of consistence, the method after Fu et al. (1998) is used, but nevertheless it may be mentioned, that the formulation after Ebert and Curry (1992) yields basically the same results. Despite of the actual relation applied, all three yield similar results to in-situ measurement in young contrails (Febvre et al., 2009).

Finally, the optical depth is determined by integrating the extinction β over a certain vertical distance.

$$\tau = \int_{z_0}^{z_1} \beta dz \tag{2.46}$$

The optical depth in Fig. 2.8 was calculated for different values of IWC, based on the same ensemble already used in the microphysics (see Tab. 2.3). Corresponding to the extinction, also the optical depth is the largest for small diameters and strongly increases with increasing IWC.

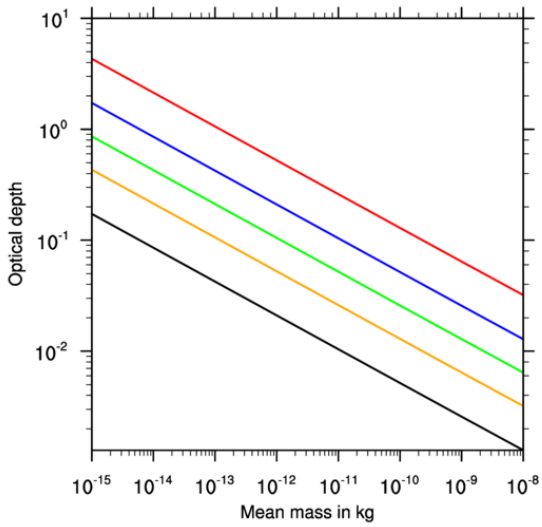

Figure 2.8: Optical depth for the solar spectrum over mean mass for the contrail radiation scheme; red: $IWC = 5.0\ mg\ m^{-3}$, blue: $IWC = 2.0\ mg\ m^{-3}$ green $IWC = 1.0\ mg\ m^{-3}$, orange: $IWC = 0.5\ mg\ m^{-3}$, black: $IWC = 0.2\ mg\ m^{-3}$.

3. Formation of Contrails

Figure 3.1: Contrails in various stages of their development, top: young, non-persistent contrail, middle: contrails in transition to contrail cirrus, bottom: young, probably persisting contrails.

3.1 The Schmidt-Appleman-Criterion for Stationary Conditions

For the forming of contrails it is not sufficient to only account for additional water vapor emitted by aircrafts that contributes to the existing budget in the atmosphere. In the middle of the 20^{th} century, scientists already discussed the question how to explain the existence of the white tail behind a streaming air plane jet. In this context, both Schmidt (1941) and Appleman (1953) pub-

lished similar theories. Schumann (1996) unified both studies and developed them to a further extent. In the following, the basic explanation is to be described briefly. Also the numerical implementation in the frame work of contrail modeling is discussed.

Usually, contrails form in the upper troposphere and lower stratosphere, respectively. In those levels, the air is relatively dry. But still, because of the low temperatures that often fall below $-40^{\circ}\,C$, already a small amount of water vapor is sufficient to cause at least supersaturation with respect to ice.

The theory behind the Schmidt-Applemann-Criterion (Schumann, 1996) is grounded on the principles of the thermodynamics. By applying several simplifications, the mixing process between two independently subsaturated air masses with different temperature and relative humidity, respectively, can be described as a linear process. For simplicity, with the formation of contrails, one assumes that the exhaust plume is at rest compared to the surrounding air. In reality, the engines of modern commercial aircrafts eject exhaust gases at velocities of about $200\ m\ s^{-1}$ (EASA, 2015). But nevertheless, it will be shown later that the error caused by this assumption is negligible.

Combustion of kerosene produces besides some trace gases and particles above all carbon dioxide and water vapor. The amount of emitted water vapor is described by an emission index EI_{H_2O} that accounts for the mass of water vapor emitted per mass of burned fuel. For the customarily used kerosene named Jet-A, this value is $1.25\ kg\ kg^{-1}$.

To derive an equation for the mixing process using similar quantities like for describing a saturation curve, first the mass of the thermodynamical system is investigated. The mass budget satisfies this simple equation:

$$1\ fuel + (N_{dil} - 1)\ air \rightarrow N_{dil}\ exhaust\ gas \tag{3.1}$$

Where N_{dil} has taken the role of a dilution factor. One mass unit of fuel burned with $(N_{dil} - 1)$ units of air produces N_{dil} units of exhaust gas.

The budget of water vapor mass mixing ratio (Δq) for the mixing plume is expressed as follows.

$$q_p = \frac{EI_{H_2O} + (N_{dil} - 1)\, q_e}{N_{dil}}, \quad \Delta q = q_p - q_e = \frac{EI_{H_2O} - q_e}{N_{dil}} \tag{3.2}$$

Here, the index p subscripts quantities describing the plume, whereas e stands for environmental variables.

Besides the water vapor, the amount of released energy is the most important parameter for understanding the formation of contrails. A jet engine operates at very high temperatures of about 500 to $600\ K$. Compared to the static energy in the environment at temperatures about $233\ K$,

the atmosphere gains a tremendous amount of energy.

The available internal energy Q depends on the used kind of fuel. A commpnly assumed value for Jet-A is $Q = 43\ MJ\ kg^{-1}$. The effectiveness η of a modern commercial aircraft engine is 0.3. Taking this into account, $\eta \times Q$ is available to the system for propulsion, whereas the rest, that is $(1-\eta) \times Q$, contributes to heat the exhaust gases. As the entire theory is based on a plume at rest, no internal energy is converted to kinetic energy accelerating the latter.

To derive an equation for the mixing line, the enthalpy (h) is treated similar to Eq. 3.2.

$$\Delta h = h_p - h_e = \frac{(1-\eta)\,Q - h_e}{N_{dil}} \tag{3.3}$$

The water vapor mixing ratio in the considered heights is rather small compared to the available vapor in the fresh plume itself. The same is true for the temperature. It is therefore justifiable to neglect the corresponding quantities accounting for the environment. Taking this into account, Eq. 3.2 and Eq. 3.3 can be simplified to:

$$\Delta q = \frac{EI_{H_2O}}{N_{dil}}, \quad \Delta h = \frac{(1-\eta)\,Q}{N_{dil}} \tag{3.4}$$

To formulate a relation that is similar to the equation after Clausius-Clapeyron in terms of the dependency on thermodynamic variables, the water vapor mixing ratio is expressed in partial pressure, whereas the enthalpy is replaced by the temperature. The last simplification seems reasonable as long as the mixing air is supposed to behave like an ideal gas. As long as saturation is not exceeded, this is justifiable.

$$\Delta q = \epsilon \frac{\Delta e_p}{p}, \quad \Delta h = c_p \Delta T \tag{3.5}$$

Here, ϵ represents the ratio of molar mass of water vapor and dry air, c_p is the specific heat capacity of air at constant pressure. To express the dependency of the partial pressure on temperature, the relations in Eq. 3.5 are divided by each others. This yields:

$$\frac{\Delta e_p}{\Delta T} = G, \quad G = \frac{EI_{H_2O} c_p p}{\epsilon Q\,(1-\eta)} \tag{3.6}$$

During the mixing process, the dilution factor N_{dil} satisfies:

$$N_{dil} = \frac{EI_{H_2O}}{\Delta q} = \frac{Q\,(1-\eta)}{\Delta h} \approx \frac{Q\,(1-\eta)}{c_p \Delta T} \tag{3.7}$$

In the last term of Eq. 3.7, the specific heat capacity is assumed to be constant because of the low surrounding temperatures. Applying, the mixing process follows a straight line in the $e_p\ -T-$ diagram between the environmental state of the atmosphere and the corresponding pair of values of the fresh exhaust plume with a slope determined by the parameter G in Eq. 3.6.

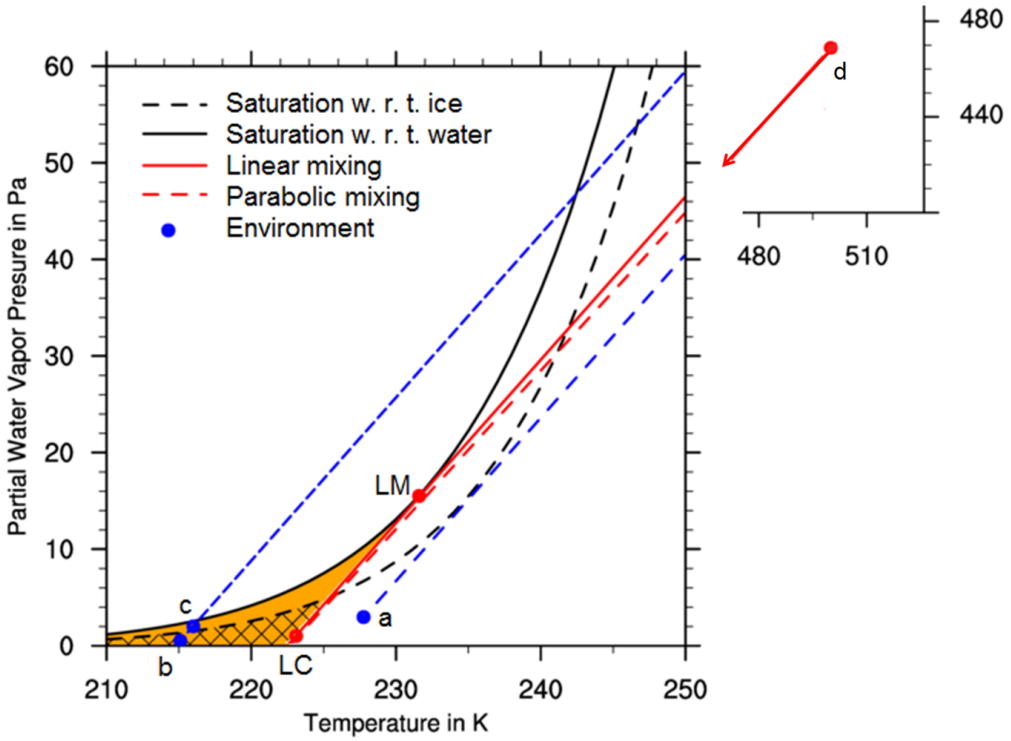

Figure 3.2: Partial pressure of water vapor over temperature with saturation curves for ice and water, respcetively, lines for linear and parabolic approximation of the mixing process, for details, see text.

Due to the exponential increase of the saturation pressure with increasing temperature, the linear mixing line may cut the saturation curve. In Fig. 3.2, the conditions and processes that lead to the formation of contrails are illustrated.

The solid black curve represents the water saturation, the curve for saturation with respect to ice is plotted in dashed black, respectively. As mentioned above, mixing of exhaust gases with environmental air can be described as a linear process. Examples for mixing lines ending at different environmental conditions, represented by the blue dots a to c and the red dot labeled LC, are depicted by the blue dashed lines and the solid red line. For completeness, the upper right panel shows the starting point of the red mixing line, characterized by temperature and partial pressure in the fresh exhaust plume.

The slope of the mixing lines is characterized by the parameter G defined in Eq. 3.6 that is calculated, using besides environmental temperature and pressure, various fuel- and engine-specific quantities. Especially the latter often are not published by the manufacturer and unfortunately, measurement under cruising conditions or in operational height are only available for few engine

types, as they are difficult and expensive to realize. But nonetheless, some reliable estimations exist (Schumann, 1996). The red line in Fig. 3.2 was calculated by assuming the fuel type JET-A and a B474 aircraft. In the actual parameterization, three different aircraft types are distinguished.

Figuratively speaking, the mixing process follows the red line starting at point d until after some time, when reaching values at the points a to c or LC, the exhaust plume is diluted to such an extent, that it is indistinguishable to the surrounding air.

The exhaust jet of the engine consists mainly of water vapor. Due to the high temperature, no droplets exist in the initial stage. For a contrail to develop, a phase transition from the gaseous to the liquid phase therefore is decisive. In contrast, it is not enough, when the mixing process only exceeds supersaturation with respect to ice. In case of saturation with respect to the liquid phase, condensation or rather homogeneous nucleation occurs. The resulting droplets freeze spontaneously by virtue of the very low environmental temperatures. Depending on the state of the atmosphere, these crystals can persist and continue growing or just sublimate again. The former leads a potentially long-living contrail, the latter produces a soon dissembling tail.

As it is crucial for the generation of contrails that the mixing process exceeds saturation with respect to water, an aircraft flying under conditions characterized by a and it's exhaust plume therefore mixing according to the lower blue line, would not form contrails. Instead, for conditions indicated by b or c, the liquid saturation is exceeded during the mixing process. Here contrails may form. Taken for granted that droplets freeze soon after their origin, an ice supersaturated environment like in c allows persistent contrails, whereas for b crystals start sublimating as they are surrounded by subsaturated air. The red solid line depicts the environmental threshold conditions. Here, the mixing line just touches the corresponding curve of liquid saturation at the critical point LM. As at LC the partial water vapor pressure is zero, this point represents the critical environmental state for a completely dry atmosphere. In a more realistic case, with $RH > 0$, it takes on values that lay on the mixing line between LC and LM. The orange shaded area beneath the curve of water saturation indicates the range of atmospheric states, where persistent contrails may form whereas in the additionally hatched area, the Schmidt-Appleman-criterion is fulfilled, but due to the subsaturation with respect to ice, ice particles sublimate, resulting in so-called non-persistent contrails.

To decide, whether the state of the atmosphere allows the formation of contrails, a critical temperature T_{LC} can be defined in such a way that environmental temperatures lower than this value allow supersaturation with respect to water. In the following, $e_{sat,l}$ stands for the saturation pressure with respect to the liquid phase.

$$T_e = T_{LC}, \quad G = \frac{de_{sat,l}\left(T_{LM}\right)}{dT} \tag{3.8}$$

Using Eq. 3.8, now the threshold temperature T_{LC} can be calculated for the threshold condition of the environmental temperature T_e being equal to T_{LC}. As the surrounding air is moist in general, but not necessarily supersaturated, the saturation deficit is accounted for with a factor $e_{sat,e}$ that represents the environmental saturation pressure weighted with the relative humidity:

$$e_{sat,e} = RH e_{sat,l}\left(T_{LC}\right) \tag{3.9}$$

Here, RH counts the relative humidity, $e_{sat,l}$ means water vapor partial pressure.

$$T_{LC} = T_{LM} - \frac{e_{sat,l}\left(T_{LM}\right) - RH e_{sat,l}\left(T_{LC}\right)}{G} \tag{3.10}$$

In case of saturation ($RH = 1$), Eq. 3.10 simplifies to:

$$T_{LC} = T_{LM} \tag{3.11}$$

The rather theoretical case of $RH = 0$ yields:

$$T_{LC} = T_{LM} - \frac{e_{sat,l}\left(T_{LM}\right)}{G} \tag{3.12}$$

In both cases, the critical temperature can be calculated explicitly. For different values of the relative humidity, T_{LM} is described only implicitly by Eq. 3.10. Here, a numerical solution considering Newton iteration is to be applied.

The following formula is an approximation for $0 < RH < 1$ (Schumann, 1996).

$$T_{LM} = -46.46 + 9.43 \ln\left(G - 0.053\right) + 0.072 \ln^2\left(G - 0.053\right) \tag{3.13}$$

A Taylor-development around the critical point LM yields:

$$T_{LC} = T_{LM} - x, \quad x = -A + \sqrt{A^2 + 2B} \tag{3.14}$$

With parameters A and B, respectively:

$$A = \frac{\left(1 - RH\right) G}{RH^2 e''_{sat,l}(T_{LM}) RH}, \quad B = \frac{2\left(1 - RH\right) e_{sat,l}\left(T_{LM}\right)}{\left(e''_{sat,l}\left(T_{LM}\right)\right)^2} \tag{3.15}$$

Here, $e''_{sat,l}$ denotes the second derivative of the saturation pressure $e_{sat,l}$.

Starting values for iteration can be obtained using the following relation:

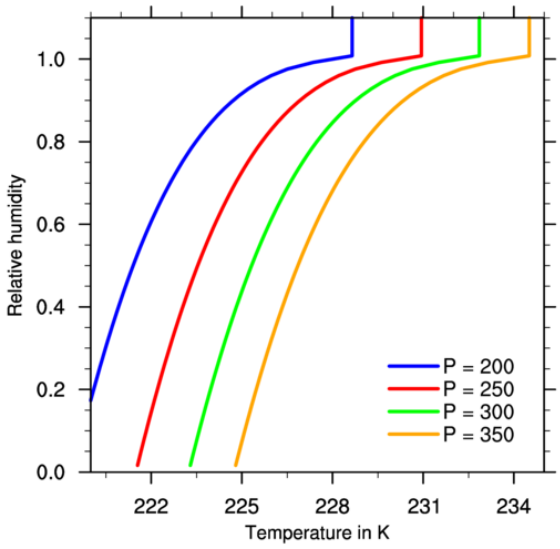

Figure 3.3: Critical temperature T_{LC} for the formation of contrails depending on relative humidity for various heights: blue: $p = 200\ hPa$, red: $p = 250\ hPa$, green: $p = 300\ hPa$, orange: $p = 350\ hPa$, $\eta = 0.3$ for all cases.

$$x^2 = \frac{2\left(e_e - e_{sat,l}\left(T_{LM}\right) + G\left(T_{LM} - T_E\right)\right)}{e''_{sat,l}\left(T_{LM}\right)} \tag{3.16}$$

Solutions exist here for $T_e < T_{LC}$. In Fig. 3.3, the example mentioned above was used for calculating the critical temperature for the formation of contrails depending on the surrounding relative humidity for various height levels, represented by different values for p. An increase of the threshold temperature with increasing values for the relative humidity is observed. For $RH > 1$, that is beginning supersaturation, the criterion is always fulfilled, as long as the surrounding temperatures are below the critical temperature for spontaneous freezing of liquid droplets. Here, a contrail will always form.

3.2 Correction for a Non-Stagnant Plume

The theory presented up till now neglects the loss of energy by virtue of converting internal to kinetic energy of the exhaust plume. This simplification now will be discussed.

The plume contains both internal and kinetic energy. The latter is partly converted into heat by turbulent dissipation, a process that causes the environmental air to be slightly warmer and the plume to cool down alike. For velocities of $v = 200\ m\ s^{-1}$, this process produces a temperature difference of about $v^2/2c_p \approx 20\ K$ in the fresh plume.

Now, replacing Eq. 3.3 yields the total enthalpy h_t:

$$\Delta h_t = \frac{Q\,(1-\eta)}{N_{dil}}, \quad h_t = h + \frac{1}{2}v^2 \tag{3.17}$$

And additionally:

$$v = \frac{F}{\dot{m}_f N} \tag{3.18}$$

Here, F represents the acceleration of each single engine, whereas $\dot{m}_f$ accounts for the fuel flow in kg per m of flight distance. The same steps like above are performed and yield now instead of a pure linear relation an additional parabolic term.

$$\Delta T = \frac{\Delta e}{G} - \frac{(\Delta e)^2}{2T_F G^2}, \quad T_f = (Q\,(1-\eta)\,\dot{m}_f)^2 c_p F^2 = \frac{(1-\eta)^2}{\eta^2}\frac{v^2}{c_p} \tag{3.19}$$

G still is the same like in Eq. 3.6, but now an effective slope can be defined:

$$G_{eff}\,(\Delta T) = \frac{d\Delta e}{d\Delta T} = G\sqrt{1 - 2\frac{\Delta T}{T_f}} \tag{3.20}$$

Considering the loss of energy due to a non-stationary exhaust plume, the mixing process satisfies the following equation:

$$\frac{de_{sat,l}\,(T_{LM})}{dT} = G_{eff}\,(T_{LM} - T_{LC}) \tag{3.21}$$

$$e_{sat,l}\,(T_{LM}) - RHe_{sat,l}\,(T_{LV}) = \Phi\,(T_{LM} - T_{LC}) \tag{3.22}$$

Where Φ is derived by resolving Eq. 3.20 to Δe.

$$\Delta e = \Phi\,(\Delta T) = G\left(\Delta T + T_f\left(1 - \frac{1-\Delta T}{T_f}\right) - \sqrt{1 - 2\frac{\Delta T}{T_f}}\right) \tag{3.23}$$

The result of these relations is depicted by the red dashed curve in Fig. 3.2. With $v = 200\ m\ s^{-1}$, temperature differences of less than $0.1\ K$ in the mean of the relevant interval for contrail forming occur. Therfore, this effect is neglected in favor of a more efficient calculation of the critical

temperature.

3.3 Initial Values for Contrails

The developed parameterization provides source terms for contrail ice by following to a large extent the contrail prediction model CoCiP (Schumann, 2012). If not indicated further, all asumptions and equations are taken from this work.

The Schmidt-Appleman-Theory predicts contrails also for only slight subsaturation, in case of very low temperatures, contrails may even from in completely dry environmental air. But without a significant supersaturation, contrails will not persist for long times. Taking a look at Fig. 3.1, persistent, line shaped contrails as well as contrails in transition to cirrus, can be seen at the bottom or middle, respectively. Short living contrails with lifetimes of seconds to several minutes (top of Fig. 3.1) do not have a measurable effect on the atmosphere's microphysics or even on its radiative budget to a measurable extent (Burkhardt et al., 2011). Therfore, as this study focuses on persistent contrails, it is not crucial to describe the initial vortex stage in a temporal exact manner. But still the knowledge of the processes taking place and the precise estimation of their effects is decisive. This is why the now presented parameterization calculates the initial height D_1 and width B_1 as well as the maximum sinking movement Δz_w in the vortex and the resulting modification of particle concentration and mean crystal diameters. After the vortex phase, at stage 1 (Fig. 3.4), it is justifiable to assume a decay of the aircraft induced turbulence to a negligible extent.

The maximum downward displacement Δz_w of a trailing vortex is mainly subject to the initial main downward vortex velocity w_0 and the stratification of the surrounding air, characterized by the Brunt-Väisälä frequency N_{BV}.

$$\Delta z_w = \frac{w_0}{N_{BV}} \tag{3.24}$$

A mean downward displacement ΔZ_1 takes into account the exhaust plume gaining buoyancy owed to the increasing temperature.

$$\Delta Z_1 = C_{z1} \Delta z_w; \quad C_{z1} = 0.25 \tag{3.25}$$

In a similar manner, the initial width D_1 is scaled, to achieve consistence to in-situ measurement in young contrails (Voigt et al., 2010).

$$D_1 = C_{D0} \Delta z_w; \quad C_{D0} = 0.5 \tag{3.26}$$

The contrail depth is approximated according to Eq. 3.27.

$$B_1 = N_{dil}(t_0)\frac{\dot{m}_f}{\pi/4\rho D_1} \tag{3.27}$$

Where the dilution factor N_{dil} follows Schumann et al. (1998):

$$N_{dil}(t) \approx 7000\left(\frac{t}{t_s}\right)^{0.8}; \quad t_s = 1s \tag{3.28}$$

To calculate the generated ice mass mixing ratio I_0 in the contrail, it is assumed that both the water vapor emitted by combustion of fuel in the engine and until further, the entire vapor contributing to supersaturation ($q_v - q_{sat}$), freezes.

$$I_0 = \frac{EI_{H_2O}\dot{m}_f}{\pi/4\rho D_1 B_1} + (q_v - q_{sat}) \tag{3.29}$$

The first term in Eg. 3.29 calculates the amount of vapor per traveled distance that is emitted because of burning kerosene. It depends on the fuel flow $\dot{m}_f$ and varies therfore based on the power of the engine. As in this study only the most common JET-A fuel used, the emission index EI_{H_2O} is set constantly to $1.25\ kg\ kg^{-1}$.

Dividing the initial ice mass mixing ratio I_0 by a constant mass for the young crystals, assuming a constant particle diameter of $d_0 = 1\ \mu m$, the number of ice particles formed is calculated. Here, the parameterization differs from Schumann (2012), where, analogous to the emission index of water vapor EI_{H_2O}, another fuel property called EI_{soot} is defined and a varying fraction of the latter assumed to act as ice nuclei. But when nucleation is thought to be homogeneous in a young contrail that offers large supersaturation combined with a huge particle number density of condensation nuclei, it is desirable to make the parameterization compute particles of equal initial diameters for each single contrail, independent on the actual extent of supersaturation. One needs to bear in mind that short-lived contrails in slightly subsaturated areas are not considered here, where different particle forming processes may be of greater importance. Also, the role of pure soot in condensation issues is inflicted with a certain uncertainty (Hendricks et al., 2005), and furthermore, a consistent description of both moments based on a single assumption seems desirable. This is why the model works with the constant initial diameter.

Finally using Eq. 3.30, the crystal loss in the wake of the aircraft (ΔI_v) is considered. By virtue of adiabatically warming (ΔT_{ad}) after Eq. 3.31 in the descending vortex, a certain fraction of the ice particles sublimates (Holzäpfel and Gerz, 1999; Sussmann and Gierens, 1999; Lewellen et al., 2001).

$$\Delta I_v = \frac{R_0}{R_1}\left(\frac{p_{sat}\left(T_0 + \Delta T_{ad}\right)}{p_1} - \frac{p_{sat}\left(T_0\right)}{p_0}\right) \tag{3.30}$$

$$\Delta T_{ad} = T_0 \frac{R_0}{c_p} \frac{p_1 - p_0}{p_0} \tag{3.31}$$

Here, R_0 is the gas constant, R_1 stands for the specific gas constant, c_p denotes specific heat capacity of air, p counts for pressure and finally p_{sat} means saturation pressure with respect to ice.

Finally, the initial mass mixing ratio of an ensemble of ice crystals that survived the vortex stage I_c is calculated using Eq. 3.32.

$$I_c = I_0 - \Delta I_v \tag{3.32}$$

The spreading and sinking is illustrated in Fig. 3.4. Depiceted is a vertical cross section of the simulated particle number concentration of a contrail for different times after generation (Unterstrasser, 2014). The red cricle in the left panel describes the initial diameter of the contrail, the red cross is the corresponding height of the centre. After about five minutes, the center has descended a distance ΔZ_1, while the cross section broadens to B_1 and D_1, respectively.

Because of the dilution (Eq. 3.33) caused by the spreading cross section of the contrail, the concentration of crystals decreases, where at the same time, in contrast to Schumann (2012), a slight growing of the particle sizes is assumed (Unterstrasser, 2014).

$$N_c = n_0 f^{1.1}; \quad f = \frac{I_c}{I_0} \tag{3.33}$$

The loss factor f yields values between 0.7 and 1.

The parameterization computes values for a contrail of approximately five minutes age. This corresponds to a descending of the center of the contrails of about $300\ m$, the horizontal extent reaches a similar size. This is comparable to measurement (Voigt et al., 2010) as well as large-eddy-simulations (Unterstrasser, 2008; Lewellen et al., 2001).

Both ice mass and particle numbers that are in a final step distributed on the entire grid cell, now serve as source terms for the microphysics scheme. The time dependency of the source terms are implicitly contained in the lenght of the trajectory treated per timestep, depending on the latter as well as on the velocity of the aircraft.

Another important difference compared to Schumann (2012) considers the online coupled calculation. The explained procedure is performed at each model time step and for each grid cell, given that both a trajectory passes by and the Schmidt-Appleman-Criterion is fulfilled simultaneously. The amount of environmental water vapor that now is contained in the recently formed contrail, no longer is available in the atmosphere. Despite of some uncertainties concerning the drying effect of contrails (Schumann et al., 2016), the simulations performed with COSMO-ART underline the

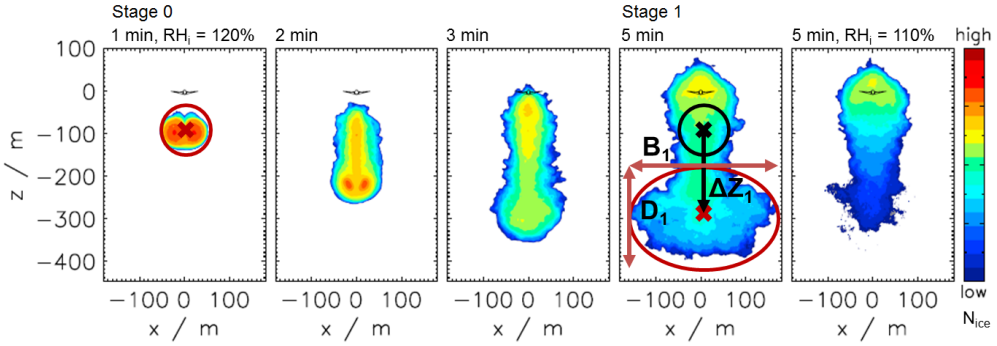

Figure 3.4: Schematic illustration of the vortex downwash, modified after Unterstrasser (2014), for details, see text.

importance of the feedback mechanism created by the online coupled setup.

The parameterization distinguishes between three different aircraft types, details can be found in Appendix C. Resulting values for produced ice mass and total particle numbers per flown distance and depending on RH_i for the various types are displayed in Fig. 3.5 (a) and (b), respectively. The right panel of Fig. 3.5 depicts the computed mean crystal radius in black. The assumed constant value of $r_0 = 1\ \mu m$ in stage 0 (Eq. 3.29) is displayed for comparison in red. As for low supersaturations, the homogeneous nucleation is not very effective, the resulting particle concentraions are smaller, resulting in larger mean diameters. This complex process is parameterized using the loss factor f in Eq. 3.33.

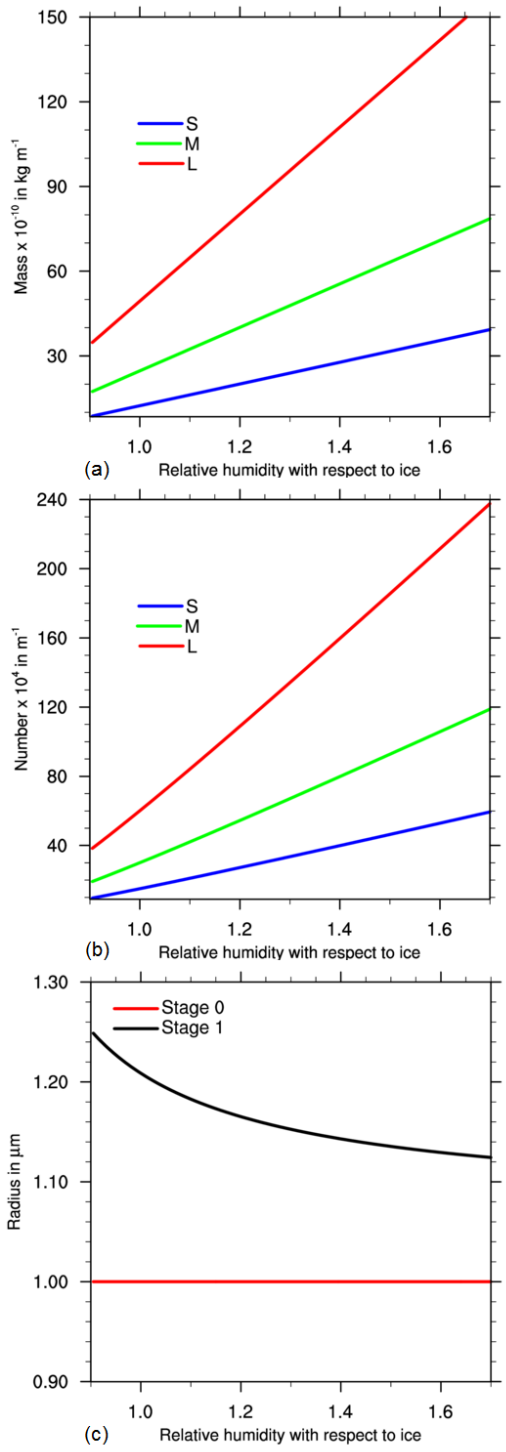

Figure 3.5: Initial values: Produced mass (a) and numbers (b) per flight distance over relative humidity with respect to ice, red for large, green for medium, blue for small sized aircraft; (c) initial crystal mean diameter mass in black, assumed $r_0 = 1\ \mu m$ in red.

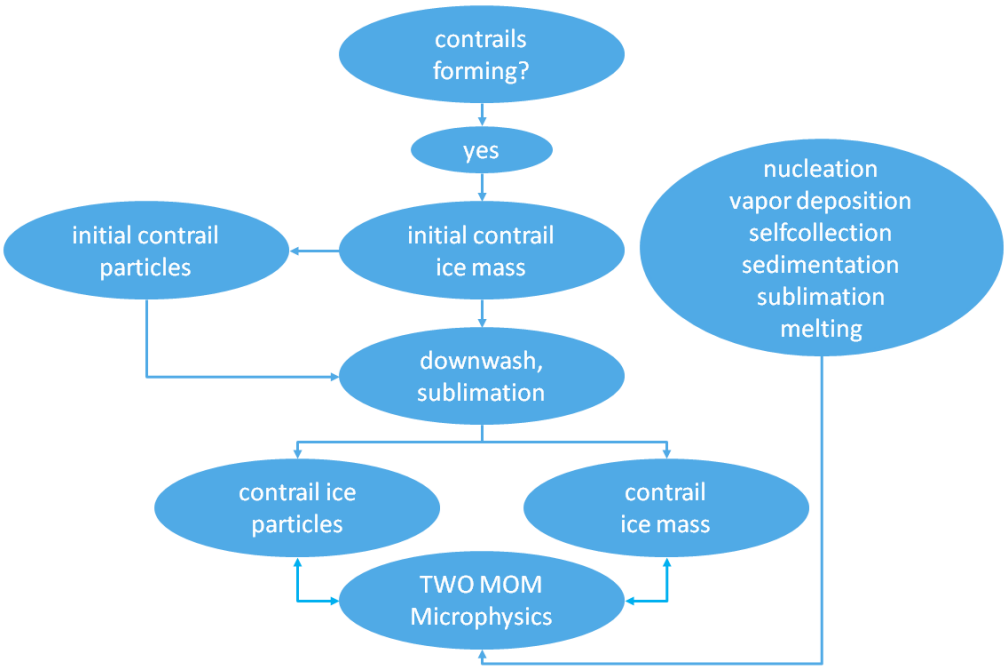

Figure 3.6: Overview of the parameterization used.

Fig. 3.6 summarizes the schematic setup of the implemented parameterization. First, the Schmidt-Appleman-Criterion is checked. In case that the formation of contrails is allowed, initial values for ice mass and number are created. The parameterization of the descending and spreading wake vortex modifies these values that finally are passed to the advection and microphysics scheme where they undergo several other processes.

3.4 Determination of Flight Tracks

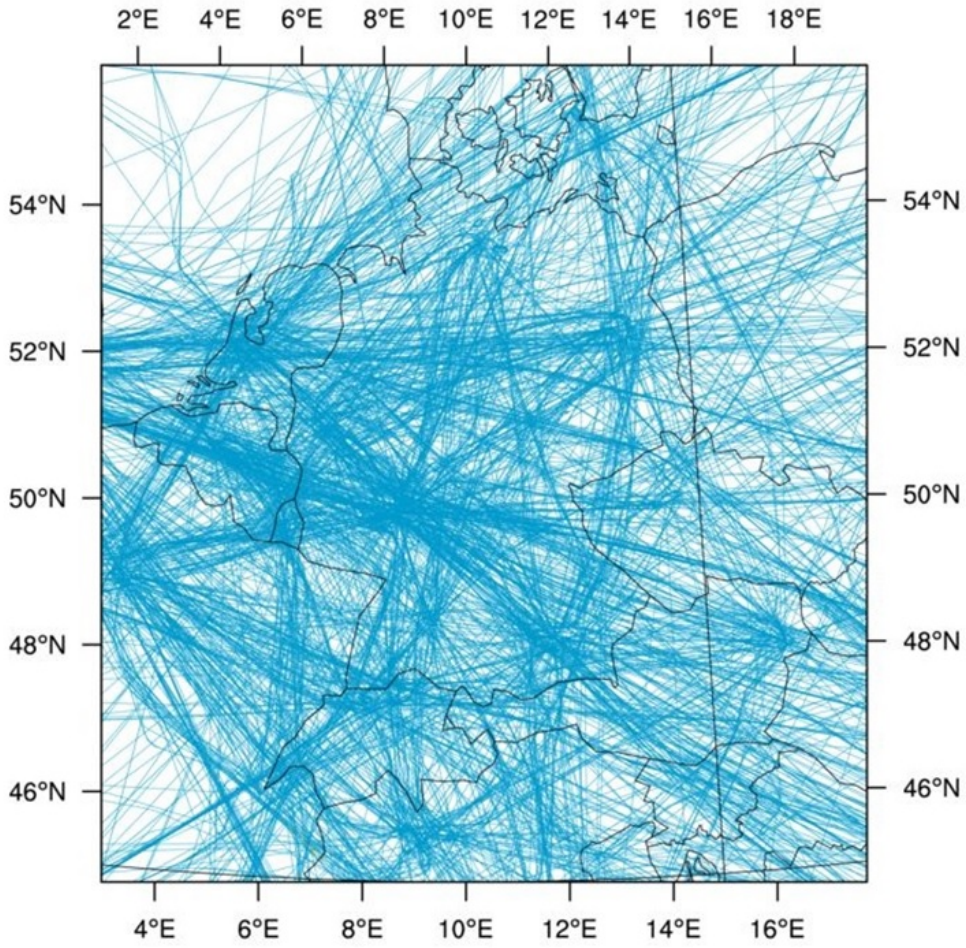

Figure 3.7: 3 December 2013, 08 UTC – 16 UTC: Trajectories for the COSMO-DE domain derived from ADS-B data.

Compared to global modeling studies, this project uses a new and recently derived data set. Instead of statistical calculations for globally averaged fuel consumption (Ferrone, 2011), the basic data consists of exact flight trajectories over a limited area that are recorded from real time based data (flightradar24, 2015) and provided by the Institute of Air Transport and Airport Research, DLR, Cologne, Germany. Besides time and geographical position of the aircraft, also information on aircraft type and current velocity is available. The total extent of the used trajectories data set is displayed in Fig. 3.7. For the test case, the data set contains eight hours of air traffic, beginning at 3 December 2013, 08 UTC and ending at 3 December 2013, 16 UTC. The corresponding data feed is depicted exemplary in Fig. 3.8. For a selected time step, each yellow plane symbolizes the current position of an aircraft equipped with an ADS-B transponding system.

Figure 3.8: 3 December 2013, $08\ UTC\ -\ 16\ UTC$: Exemplary data feed.

As the ADS-B project is not only consisting of a professional network for data collection, both temporal and spatial accuracy have to be treated carefully (Schumann, personal communication). But still, over large parts of Europe, the temporal resolution is about one minute, while the trajectories are resolved with a horizontal accuracy spreading from $1.5\ km$ to $15\ km$. Large derivations of up to $15\ km$ are mainly owed to the influence of flying in strong winds or at landing (flightradar24, 2015).

Also, the completeness for representation of the commercial air traffic cannot be stated with security. About $75\ \%$ of all commercial passenger aircraft in Europe are equipped with an ADS-B transponder and about $99\ \%$ of Europe is covered with ADS-B receivers (flightradar24, 2015). But nevertheless, as the amount of trajectories still is huge as shown above, this project focuses on a correct treatment of the microphysical and radiative processes involving contrails rather than on a most accurate representation of the actual aircraft position, as the former is a lot more vital for the prediction of contrails, their influence on cirrus cloud coverage and the impact on the atmosphere's radiative budget. Nevertheless, the trajectories are the only source of information this study can rely on and are still more exact than the initial information former studies were based on. As the following chapter will show, the ADS-B data provides a suffcient number of flights, a certain deviation in terms of temporal or spatial exacteness is negelectable, as it seems more important to focus on the description of the processes taking place while a contrail is formed.

The trajectories are interpolated to a $1\ km\ \times\ 1\ km$ grid, in the vertical direction the data is distributed with the accuracy given to the center of the corresponding model layers. This method may cause vertical differences up to $300\ m$, but at the same time avoids aliasing effects as the main flight levels lay often at the margins of two neighboured vertical model layers.

A commercial aircraft at cruise reaches velocities up to $900\ km\ h^{-1}$, combined with the $25\ s$ time

step and a horizontal mesh size of $2.8\ km$, roughly two grid cells are passed within one model time step. Therfore, the trajectories are treated in intervalls, covering a lenght that correspondens to the mean travelled distance during one time step. In case of a contrail forming, the produced ice in units of mass or number per distance and time step is distributed over the entire intervall.

4. Case Study

In the former chapters, a parameterization for treating contrails in the regional weather prediction model COSMO-ART was described. To test the developed methods, a case study is performed. Examining various sources of satellite images, a situation that stands out because of its high density of contrails combined with apart from those mostly cloud-free conditions was chosen.

In the following, first the synoptic situation of the selected test case is described. Afterwards, the microphysical and optical properties of the simulated contrails as well as their interaction with natural ice clouds are investigated. The last part consists of a description of the overall change in the radiative budget of the atmosphere due to contrails and contrail cirrus and an estimation of the impact on the gain of photovoltaic systems.

4.1 Synoptic Situation and Model Setup

The developed methods are applied for one single day (3 December 2013). On this day, the meteorological conditions over Central Europe were favorable for the formation of contrails. Additionally, the natural high cloud coverage was relatively low, facilitating the identification of contrails on satellite images. The simulation is performed on the COSMO-DE domain, which mainly covers Central Europe. Fig. 4.1 shows the synoptic and geographic situation for this simulation.

Except for a thick cloudbank over the North- and Baltic Sea and some fog over Southern and Western Germany, a great number of line shaped contrails and diffuse cirrus clouds can be seen. Especially the last-mentioned consist in large measure of contrail cirrus and contrail induced cloudiness as will be shown later. A main contrail-supporting area is found over Central Germany, probably corresponding to the airport of Frankfurt. Other expanses can be seen over the Netherlands and Belgium, over the Czech Republic and South of the Alps.

The model setup is differing from the standard (Baldauf et al., 2011), as a horizontal mesh size of $2.8 \times 2.8\ km$ and 80 vertical levels reaching up to elevations of $\sim 20\ km$ are used. The high resolution was chosen in a way, that in the important vertical sector between $9\ km$ and $12\ km$ at least every $300\ m$ one model layer is present. For comparison, the levels in a standard con-

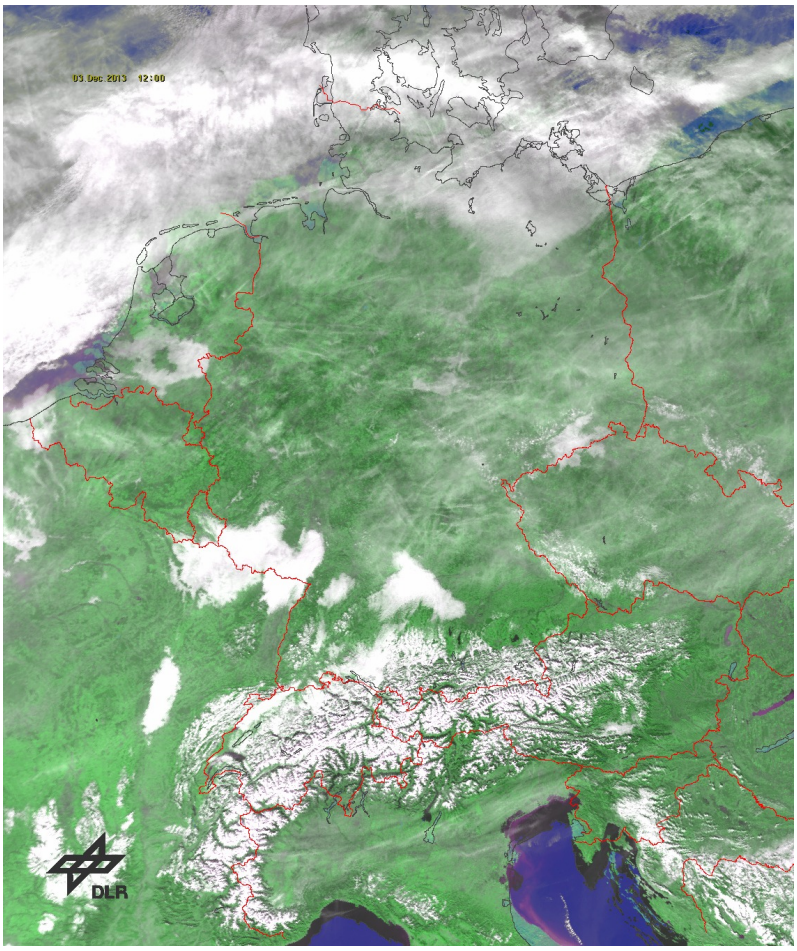

Figure 4.1: Satellite product for Central Europe, 3 December 2013, 12 UTC.

figuration spread out here with about 700 m, which is a typical distance between the main flight levels. Because flight levels lying more or less exactly on model layers are double counted or even vanish during the interpolating procedure, the higher resolution helps to minimize theses aliasing effects. Besides, the model does not operate with fractional cloud coverage. That is to say, in case of cloud formation, the ice is dispersed evenly over the entire volume. In contradistinction to the description of natural clouds, this is an issue to deal with in contrail modeling. Especially larger vertical grid spacing would force contrails to instantly spread across the entire vertical extent of the cell. This in turn causes unrealistic high dilutions of the ice particles and a strongly underestimation of both the microphysical and optical effects of contrails and contrail cirrus.

To take into consideration the large velocities of commercial aircrafts at cruise and to maintain the stability of the model while using the two moment cloud microphysics scheme, a rather short integration time step of $\Delta t = 25\ s$ is chosen, indicating, an aircraft passes on average two grid cells per time step. A possible vagueness with respect to the calculated initial ice that is calculated

in mass per distance, is reduced.

For meteorological boundary data, COSMO re-analysis with a coarser resolution of $7.5\ km$ $\times\ 7.5\ km$ are used. The formation and further development of contrails is very sensitive to the either super- or subsaturation of the surrounding air masses. Despite a young contrail is comparable to cirrus clouds with regard to the ice mass mixing ratio, appearing crystal diameters are a lot smaller. Therefore, already slight subsaturations cause an entire contrail cluster to sublimate within few time steps. To correctly predict contrail coverage and evolution, the meteorological conditions and their variety in the upper troposphere need to be captured with high accuracy. Since there is no in-situ measurement for contrails or contrail cirrus available, satellite images and radio soundings serve for general validation purposes.

A comparison of the model output and the radio sonde at the Lindenberg Observatorium for 3 December $2013,\ 12\ UTC$ is displayed in Fig. 4.2. Both simulated and observed temperature, depicted in the right panel, are in very good agreement up to the top end of the model domain. Also, the amount of available water vapor in Fig. 4.2 (b) match, despite for an area between in the lower troposphere, where the model does not to represent the large variation of the water vapor mixing ratio with height. But nevertheless, the model computes comparable values in the main contrail developing region that is located far above the poorly represented area, roughly between $400\ hPa$ and $200\ hPa$. The same behavior is seen for the relative humidity with respect to ice in Fig. 4.2 (c) that is the most crucial meteorological quantity for contrail formation and persistence, as explained during the previous sections. In the upper troposphere, the model slightly underestimates the saturation, but the overall picture is a reasonable agreement. Addressing Schumann (2012), where ECMWF data is used, while COSMO analysis are said to not represent humidity in a satisfactory way, it can be shown, that COSMO does really well, at least at the chosen situation and the applied fine resolution.

The measurement at Lindenberg can help to understand the reasons for the high density of contrails and the concomitant absence of natural cirrus in the satellite image (Fig. 4.1). For the generation of cirrus clouds, besides an upward moving air mass, also a strong supersaturation with respect to ice of about 1.4 to 1.6 is necessary. The relative humidity determined by the measurement of the radio sonde lies between 0.9 and 1.2 in the upper troposphere and is too low for allowing a widespread formation of natural cirrus. As the processes that produce persistent or at least visible contrails require much lower supersaturation, these conditions are fulfilled at this situation.

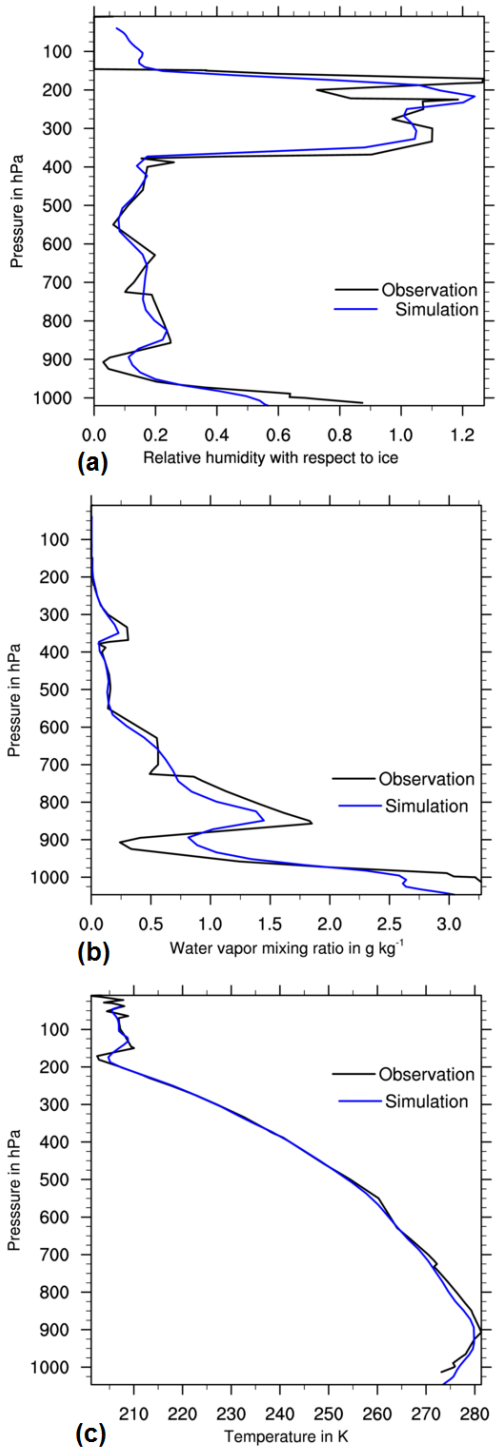

Figure 4.2: Model output and radio sonde profiles at Lindenberg, 3 December 2013, 12 UTC: (a) Relative humidity with respect to ice, (b) Water vapor mixing ratio, (c) Temperature.

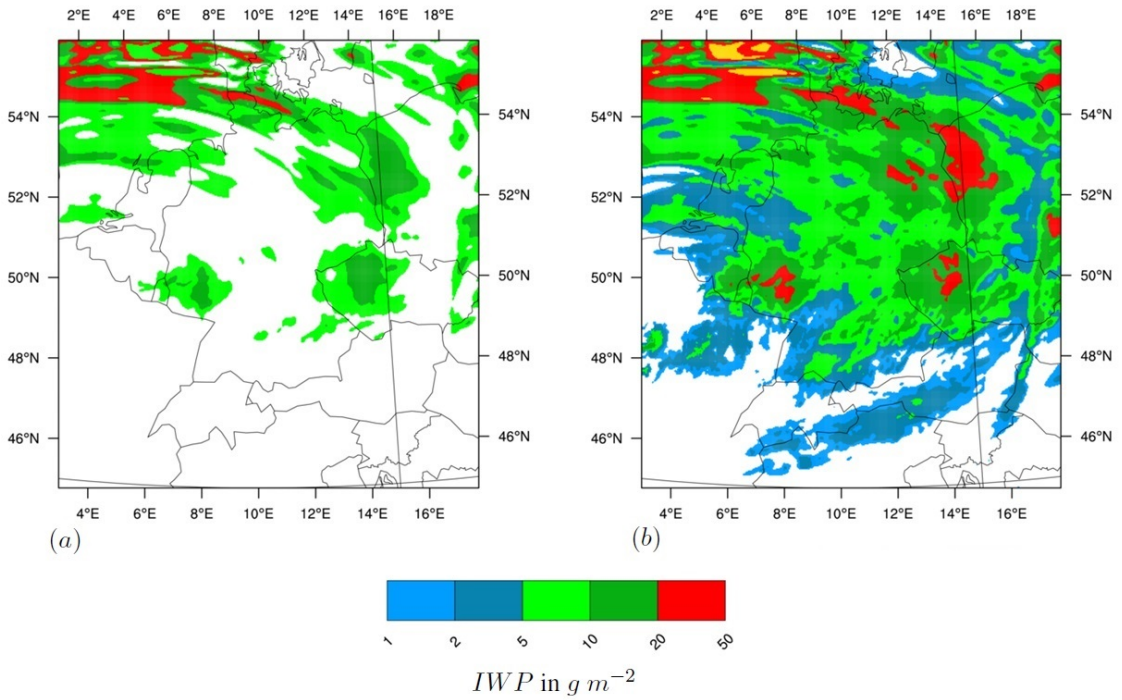

Figure 4.3: 3 December 2013, 10 UTC: Ice water path from the reference simulation (a) and for a simulation with contrails (b).

4.2 Microphysical Properties of Contrails

This section is dedicated to the microphysical properties of the simulated contrails. Alongside others, one of the central questions of this study is, whether considering contrails improves the representation of high level cloud coverage in a numerical weather prediction model. As suspected, contrails scarcely cause precipitation or impact the large scale wind field. Nonetheless, they are of a certain importance for high level cloud coverage and the arising differences in the radiative budget of the atmosphere. Therefore, first the simulated ice water path (IWP) is investigated. This quantity measures the amount of ice present in a column, usually looking in a vertical direction.

The overall IWP is computed using the following formula:

$$IWP = \int_{z=0}^{\infty} \rho \, IWC \, dz \tag{4.1}$$

With ρ symbolizing the density of moist air.

Fig. 4.3 compares the total ice water path for natural ice in the reference run without contrails (Fig. 4.3 (a)) and a simulation where the contrail parameterization is switched on (Fig. 4.3 (b)).

The second contains both natural and contrail ice, including young contrails and contrail cirrus. The time of the observation is chosen in accordance with the satellite image (Fig. 4.1) to allow a qualitative validation.

The reference run produces a rather thick bow structure over the North Sea reaching to the eastern boundary of the domain. Two minor areas covered with cirrus are found over Western Germany and the Ukraine.

Evidently, the overall pattern of cloud coverage changes significantly when taking the effect of aircraft induced clouds into account. The preexisting structures are intensified, although there might be a slight overestimation as values of IWP up to 20 to 50 $g\ m^{-2}$ are quite high. Additional cloud coverage over the entire simulated area is in good agreement with the presented satellite image (Fig. 4.1). The line shaped structure of young contrails is not visible in the IWP by virtue of the integration over a large vertical distance, but nevertheless, the high cloud coverage over Germany, Poland and the Ukraine is mainly caused by the existence of contrails in various stages of their life cycle.

An interesting feature can be observed south of the Alps. The reference run predicts no cirrus here, although a thin veil can be seen in the satellite image. In contrast to the reference, the contrail simulation contains values of IWP about 1 to 5 $g\ m^{-2}$ here. The same is true for areas located over Germany and Western Europe. The airport of Frankfurt is the major hub for European and transatlantic commercial air traffic. The high number of connections and a corresponding high frequency of aircrafts passing over that area, metaphorically speaking cause one single exhaust plume over the region. To a minor extent, a similar situation is observed over airports located in Western Europe.

4.2.1 Young and Aged Contrails

Concerning their microphysical properties, contrails differ strongly from natural high clouds. Cirrus clouds occur in strong supersaturation, when a slight ascending movement of the surrounding air is present. Because of the high supersaturation, homogeneous nucleation is inhibited. Instead, particles that are large and ensue in low concentrations form heterogeneously. At the margins of a cloud, caused by local downward movements or simply because of the large crystals' sedimentation velocity, fall streaks form, observable in so-called cirrus virgae.

In contrast, contrails would form in air at rest and even in a completely dry environment, provided that temperatures are sufficiently low. The exhaust plume makes a huge amount of condensation nuclei available, common values assumed for the soot particle number concentration per unit of burned fuel (EI_{soot}) are in the order of $10^{14}\ kg^{-1}$. Apart from this, the temperature in the favorable surrounding often lays beyond the point of spontaneous freezing. Finally, given that the

plume is subsaturated and very hot, the mixing process described with the Schmidt-Appleman-Criterion, offers sufficiently low supersaturations to favor homogenous nucleation in the early stage of contrail forming. This is why a young contrail consists of very small particles with radii of about 1 to 5 μm and high number concentrations up to 150 cm^{-3}. Owed to their small size, settling velocities are small, too, indicating that sedimentation is an ineffective sinking process and fall streaks are unlikely being observed at least in young contrails.

Fig. 4.4 shows in (a) the ice water content (IWC), in (b) the particle number density (N) and in (c) the volume radius (r_v) for the simulated contrail ice in the layer of 10 300 m height for the chosen day at 10 UTC. The maximum contrail age at this point is two hours. At this time, they still consist of lots of very small ice crystals. As explained before, the dominant microphysical process modifying a contrail ice ensemble is growing by deposition of water vapor. In case of subsaturation, the particles sublimate within few time steps.

Independent of the regarded quantity in Fig. 4.4, the line shaped structure of young contrails can be easily seen. The number densities in Fig. 4.4 (b) lay often above 100 cm^{-3}, whereas the calculated particle radii (Fig. 4.4 (c)) with values between 1 and 5 μm are about one order of magnitude smaller to what is observed in natural cirrus. Contrary to these deviations from natural cirrus properties, the average mass density of the young contrails in Fig. 4.4 (a) reaching from 0.3 to 3.0 $mg\ m^{-3}$ is comparable to thin cirrus clouds.

In Fig. 4.4 (c) to (f), the same quantities like Fig. 4.4 (a) to (c) are depicted, but for a situation three hours later. Therefore, some contrails are now up to five hours old and find themselves now in a phase of transition to contrail cirrus. Deposition of environmental water vapor made them grow, the mean particle radii is about one order of magnitude larger in Fig. 4.4 (f) compared to Fig. 4.4 (c). Also, larger particles start to depose themselves. Since a particle falling through a supersaturated air mass experiences strong growth owed both a certain increase of available water vapor for further depositional growth and effective collection processes. Comparing Fig. 4.4 (a) and Fig. 4.4 (d), only small changes in the ice water content are observed. Obviously, because of the persistent supersaturation with respect to ice over vast areas of the domain both horizontally and vertically, no significant loss of mass caused by sublimation takes place. On the other hand, the number density decreases strong in Fig. 4.4 (e). Here, besides the already mentioned sedimentation process, advection causes a certain dilution and additionally, particles join to each other, reducing the absolute number of an ensemble.

Figure 4.5 illustrates the vertical layering of the simulated contrails with displaying a longitudinal cross section through the contrail cluster, located the center of the domain, indicated by the red line in Fig. 4.4 (a). The top left panel shows the ice water content of the cluster reaching the highest values about 10 300 m above ground. In addition, several maxima of particle concentration

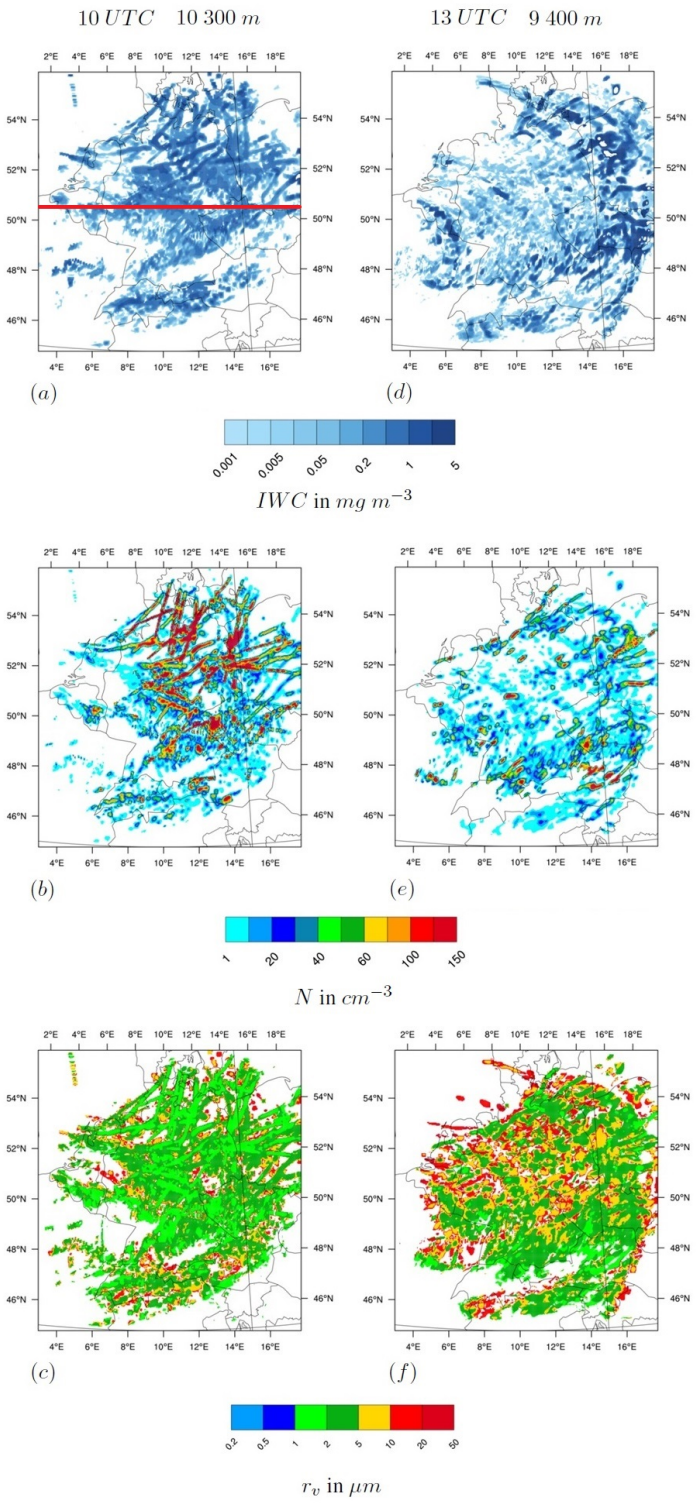

Figure 4.4: Properties of young and aged contrails, left column: 10 UTC, 10 300 m, right column: 13 UTC, 9 400 m; top row: ice water content, center: particle number concentration, bottom: volume radius.

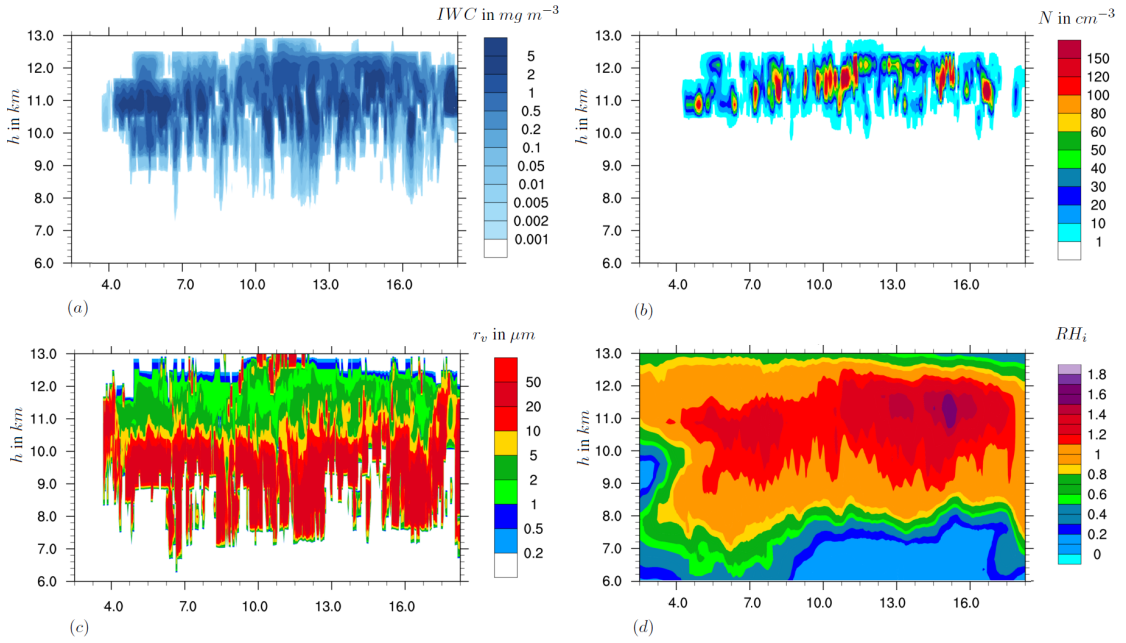

Figure 4.5: 3 December 2013, 12 UTC: Vertical cross section through contrail cluster: (a) ice water content in, (b) particle number concentration, (c) volume radius, (d) relative humidity with respect to ice.

are located in these regions (Fig. 4.5 (b)). Consequently, the mean particle radii (Fig. 4.5 (c) here are remarkably small, spreading from 1 to 5 μm.

This constellation of high number densities and small particle diameters is observed in the horizontal plots (Fig. 4.4) as well and was identified as young, line shaped contrails. Basically, each local maximum, clearly separated from the next in Fig. 4.5 (b) belongs to a single, recently formed contrail.

The major reason for the high density of contrails in heights between 9 km and 12 km is to a certain extent of technical origin. In these heights, the main flight levels are located. Despite for serious reasons, commercial aircraft do no climb higher. Given they would, as proposed by several mitigation studies (Ferrone, 2011), the overall picture would look very different. The relative humidity with respect to ice, displayed in Fig 4.5 (d), shows strong supersaturation in the vertical area with the most dense air traffic. Above, values of RH_i drop rapidly with height, indicating the position of the tropopause. In case of aircrafts cruising in these regions, contrails would form due to the low temperatures, but vanishing soon, as ice particles cannot exist in subsaturated air.

The vertical distribution of the microphysical properties shown in Fig. 4.5 (a) to (c) reveals more details about a contrail life cycle. Obviously, the environment in the entire domain is supersatu-

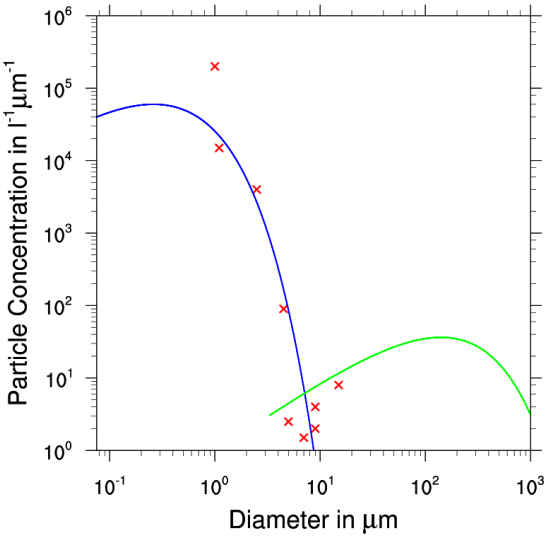

Figure 4.6: Size distributions of simulated ice particles in young contrails (blue) and contrail cirrus (green); red: measurement in young contrail (Febvre et al., 2009).

rated between heights of 7 km to 13 km, offering favorable conditions for both contrail forming and contrail persisting, but as the relative humidity hardly ever exceeds 1.4, natural cirrus clouds would not form in a significant extent. The vertical distribution of the particle mean radii is stratified vertically. In the main developing region between 11 km and 12 km height, the smallest crystals exist, whereas a strong increase of the particle sizes is observed with decreasing height. As the young contrail ice crystals are too small to be sedimented, they remain in the level of origin until the sublimate or have grown by deposition of environmental water vapor to such proportions, that sedimentation is starting to be an effective sink. The analyzed cluster in Fig. 4.5 consists of contrails that are up to 4 h old. The oldest and largest particles started already to fall and undergoing the processes described above. The abrupt bottom end of these fall streaks match to the border between super- and subsaturation in Fig. 4.5 (d). Further descending leads inevitably to sublimation. The simulated stratification with respect to mean particle radii is in good agreement with both model studies (Unterstrasser, 2008) and measurements (Voigt et al., 2010).

Without measurement, validation of the simulated contrail properties is rather difficult. Nevertheless, Fig. 4.6 presents a comparison between the calculated spectra and measurement in a young contrail (Febvre et al., 2009).

For the blue curve in 4.6, an area of about 5 km x 5 km covered with young contrails was averaged. The size distribution has a maximum for diameters around 0.5 μm, the peak for smallest measured particles is observed for values around 1.0 μm. As the used instrument did not capture lower mean diameters (Febvre et al., 2009), no direct comparison is possible here. For larger

mean particle diameters, the model agrees in a reasonable manner with the measured particle concentration. Of course, these two spectra are not to be compared exactly, as the actual meteorological situations may be entirely different. Also, a contrail changes its appearance in the first few minutes very strongly. That is to say, comparing measurement and simulation reveals that the first is a contrail that is just in the process of development, whereas the simulated cluster, that necessarily was averaged to gain enough information, besides very young also contains slightly aged contrails. But nonetheless, the same general shape and a corresponding order of magnitude can be seen both in simulation and observation.

The green line in 4.6 refers to another area of similar size, but now containing contrails that are in their transition state. In these mature contrails, the very small particles are not present anymore. Instead, a maximum around $100\ \mu m$ arises. These values are comparable to natural cirrus crystals, except for a higher concentration. Here, a rather thick contrail cirrus is about to form. Although measurement is only available for the bottom end of the size distribution, at least here a reasonable agreement is present, although the model seems to slightly overestimate the particle concentration.

4.2.2 Influence on Cirrus Clouds, Contrail Induced Cloudiness

Besides investigating contrail microphysical properties, the developed model configuration allows also the examination of the direct influence of contrails on the naturally occurring high cloud coverage. A goal of this work is to quantify the changes in the atmosphere's radiative budget. Hence, it is crucial to have a look at the interaction of contrails and cirrus, as differences in the amount of received radiation at the surface arise mostly from alterations in both the cloud coverage and the ice water content. Obviously, increased cloud coverage or a thicker cloud prevents solar radiation from reaching the ground more efficiently than few or thinner clouds would do.

The contrail microphysics is treated separately from the one for the natural ice phase, but nevertheless, feedbacks are allowed. For example, both hydrometeor classes can compete for the available amount of water vapor. Rather for technical reasons, contrail particles exceeding a certain threshold concerning the mean mass are subsequently treated along with the natural ice. The threshold is chosen in a way that virtually no difference in terms of the mean particle diameter is existent any more. An increase in natural ice mass and number concentration, respectively, is interpreted as contrail induced cloudiness. This type of artificial cloud cannot be distinguished from natural cirrus by detection algorithms for satellite products. But nevertheless, concerning their effect on radiation, they are not comparable to natural cirrus owing to the still smaller mean particle diameters and the larger number densities.

Fig. 4.7 displays the difference in natural IWP for two simulations. The values from the reference run are subtracted from the results of the simulation with the parameterization switched on. The red, line shaped structures consist of additional ice particles, that originally occurred in

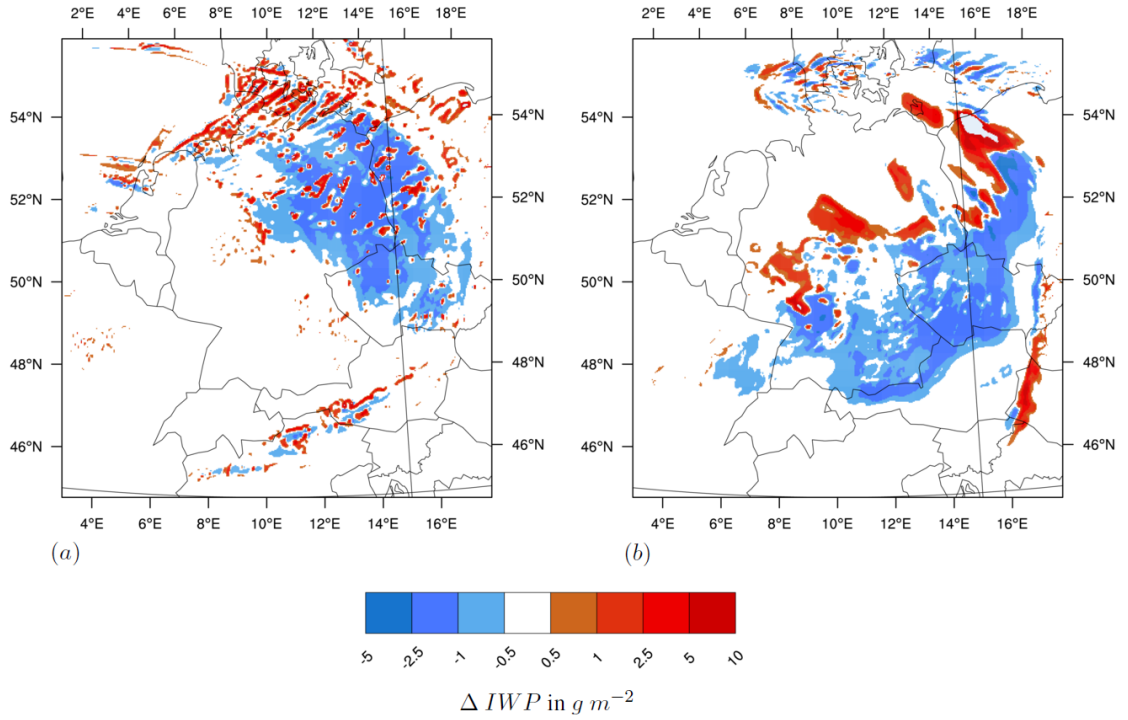

Figure 4.7: 3 December 2013: Difference in natural ice water path for simulation with and without contrails, (a) 12 UTC, (b) 17 UTC.

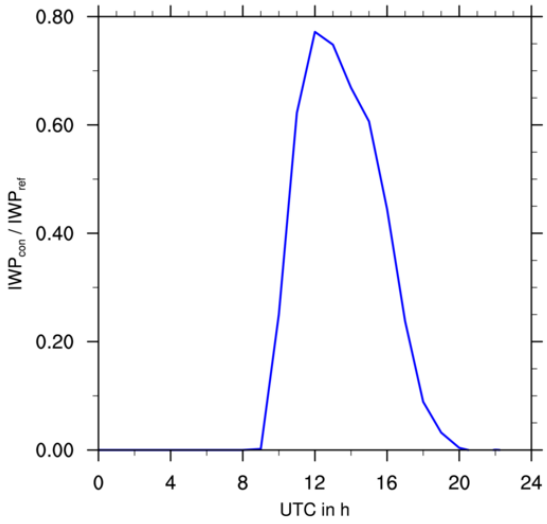

Figure 4.8: Temporal evolution of the spatial mean ratio between contrail induced ice mass and the total ice mass.

contrails but grew in such a dimension, that their mean diameter or rather the mean mass of an ensemble now is as large, to be treated like natural crystals. Negative values in blue indicate a reduction in natural cloudiness because of existing contrails. As contrails and contrail cirrus contain water vapor, that now cannot neither be transported nor serve to form cirrus. The left panel of shows the situation at 12 UTC. A clear increase of cirrus-like cloudiness is seen with mostly line shaped patterns, indicating a growth of particles especially at the margins of the contrails. The large area over the east of the area is dominated by bluish colors. Here, contrails have a dehydrating effect, contrary to other studies (Schumann et al., 2015).

The effect is even enhanced at later times, where an overall negative influence of contrails on the high cloud coverage is seen (Fig. 4.7 (b)). The negative impact of contrails on natural cloudiness by consuming water vapor that was available for cirrus beforehand, does not or only to a small locally limited extent reduces the absolute high cloud coverage. In general, as seen in Fig. 4.3 (b) a strong total increase is observed. Only the vapor is redistributed for the good of contrails. Taking into account the differing microphysical properties, especially the much smaller particle sizes, this phenomenon influences the impact of incoming radiation to a certain dimension.
The influence of contrails on the composition of high level clouds can also be described by investigating the modification of the overall cloud coverage. An equal depiction is the spatial mean ratio between the contrail ice mass and the total ice mass in a reference simulation. Fig. 4.8 shows the temporal evolution of this quantity. After about an hour after the first contrails have formed, a remarkable fraction of the total ice water content of the investigated domain consists of contrail ice, the maximum is reached at 12 UTC, when nearly 80 $\%$ of all ice present in the upper troposphere is aviation induced, either formed directly from aircraft exhausts or grew of the latter

by deposing environmental water vapor, replacing natural cirrus clouds.

4.3 Optical Properties of Contrails

In the past section (Section 2), not only a separate treatment for contrails concerning their microphysics was described, but also a contrail radiation scheme was presented. As ice particles in a young contrail differ from natural ice not only in their high number concentration but also in their shape, this special treatment is necessary to correctly quantify both the radiative properties and the resulting influence on the radiative budget.

4.3.1 Effective Radius

The horizontal distribution of the contrail effective radius r_e over the whole domain is displayed in Fig. 4.9. The top row shows the situation at $09\ UTC$, when the maximum age of contrails is one hour. In Fig. 4.9 (a), r_e in $11\ 300\ m$ is shown. In this height, the majority of contrails are formed, as this layer contains the main flight levels. Especially in the young and therefore still narrow and line shaped contrails, the effective radii of ice particles usually do not exceed $8\ \mu m$, in areas with lower particle number density, such as at the margins of the single trail and the contrail cluster itself, larger values up to 12 to 15 μm occur. For the same time, but $1\ 700\ m$ below, Fig. 4.9 (b) shows nearly the same pattern in terms of spatial distribution, although here, much larger effective radii are observed. Mean values spread around 12 to 20 μm. This downward increase of r_e is consistent with the presented r_v in Fig. 4.4 as well as the vertical evolution in Fig. 4.5. The same behavior also was observed in former studies and observations (Jensen et al., 1998a).

Some minor line shaped structures with low values for r_e are related to recently formed contrails in this layer. To be mentioned again, a certain part of the simulated contrail ice particles is missing in this depiction of the effective radius. As described in Chapter 2, particles with $r_e < 2\ \mu m$ are not taken into account to secure convergence of the radiation scheme. Nevertheless, the effective radii presented here describe not only the small contrail ice particles. Also, additional ice in the cirrus ice class is considered, representing the contrail induced cloudiness.

The bottom row of Fig. 4.9 shows the effective radii for the same heights but at $16\ UTC$, corresponding to a maximum contrail age of eight hours. At this time, basically no new contrails are formed anymore. Although, the general pattern of decreasing particle sizes with height still appears, the effect is of much smaller extent. An increase from 4 to 6 $\mu\ m$ in the upper layer to about 8 to 10 μm in the lower level is observed. The contrail cirrus pattern over the center and the eastern part of the domain consists of nearly uniform sized particles in both height levels. The larger crystals that are present in Fig. 4.9 (b) are large enough to experience sedimentation. In addition, both vertical and horizontal mixing contributes to this homogeneous distribution of contrail ice particles.

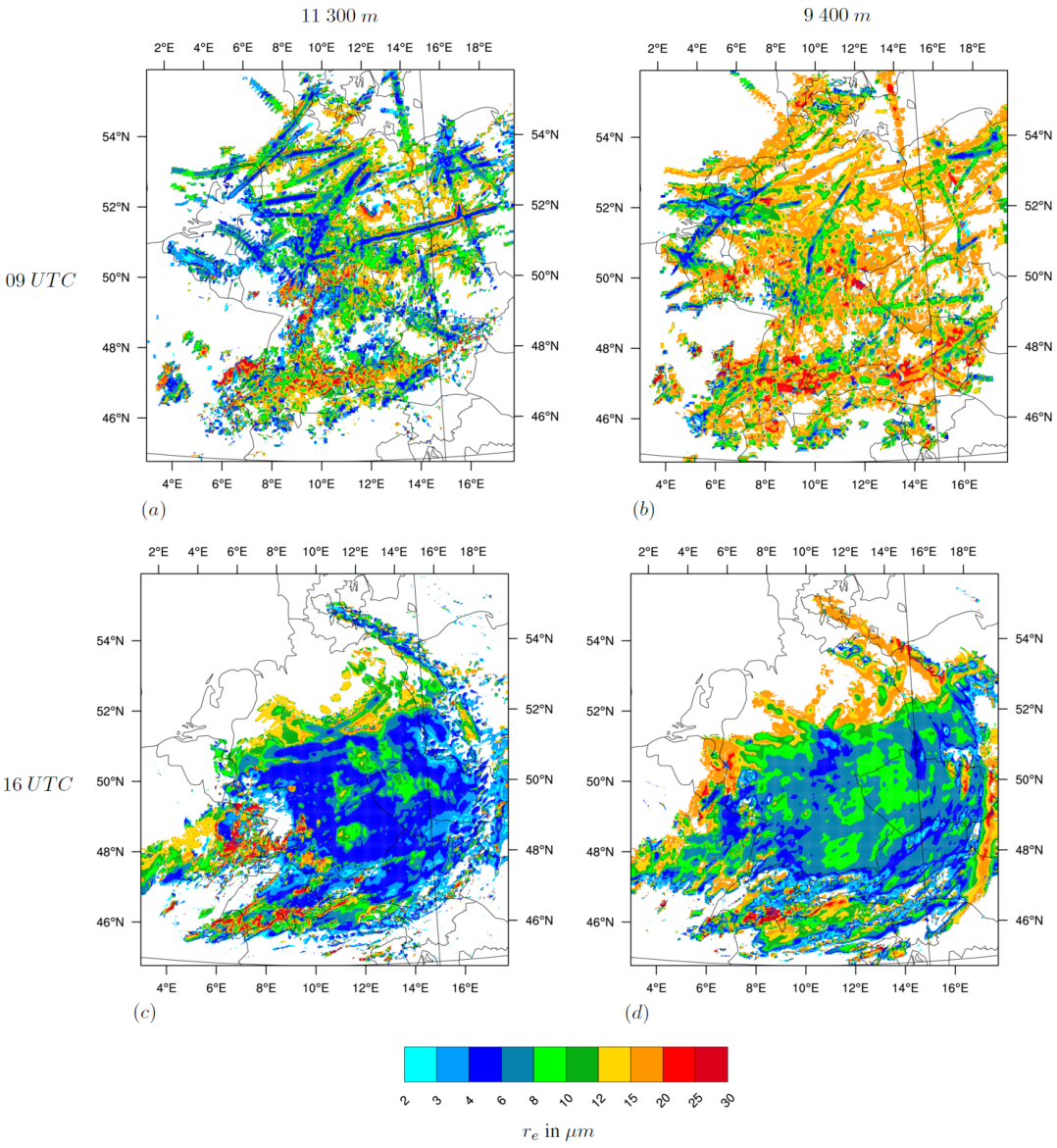

Figure 4.9: Contrail ice particle effective radius: 09 UTC (top), 16 UTC (bottom); left column: 11 300m, right column: 9 400 m.

4.3.2 Optical Depth

The crucial quantity for estimating the direct impact on the radiative budget of the atmosphere is the optical depth τ of contrails. By virtue of the overall small particle radii, both young and rather aged contrails are comparable to thin natural cirrus with respect to their optical depth.

The top row of Fig. 4.10 depicts the optical depth for the same time and heights like Fig. 4.9 (a) and (b). The optical depth of a vertical column is calculated by integrating the extinction between two considered height levels. It has to be mentioned that here the optical depth is calclulated only for one single model level and not for the total height of a contrail or contrail cirrus, a slight underestimation compared to measurement that take into respect the total thickness of a cloud. As the extinction depends on both the effective radius and the ice water content, of whom the latter is decreasing with increasing height, τ is small in higher levels. Therefore, in the upper levels (Fig. 4.10 (a)), the optical depth of young contrails is about 0.01 to 0.04, increasing to values up to 0.2 in the height of $9\ 400\ m$ (Fig. 4.10 (b)). These results are in reasonable agreement to large-eddy-studies (Unterstrasser et al., 2010) and in-situ measurement (Voigt et al., 2010). As they start to spread during the day, the overall density of contrails is largest around noon. The contrail optical depth for $13\ UTC$ is shown in the middle row of Fig. 4.10. In the upper level considered (Fig. 4.10 (a), both a spreading and a quantitative increase of optical depth is observed. Small contrail ice crystals, that are not sedimented, can accumulate and form rather thick contrail cirrus. Also in lower heights, contrail and contrail cirrus coverage increases in thickness (Fig. 4.10 (b)) and the optical depth reaches values of up to 0.6.

Finally, the optical depth of contrails at $16\ UTC$ is depicted in the bottom row of Fig. 4.10. At this time, contrails are not line shaped anymore, as seen above, they now are in a state called contrail cirrus or rather contrail induced cloudiness, respectively and form a coherent cluster that is advected to the south of the domain by the atmospheric current. As the optical depth depends on the microphysical properties, as discussed above, is undergoes the same development of sedimentation, collection processes and sublimation, resulting in a decay of the optical depth to values between 0.02 and 0.2.

To summarize these results, Fig. 4.11 displays a cross section for both discussed quantities, the effective particle radius and the optical depth. The position of the cross section is located the center of the domain, indicated by the red line in Fig. 4.4 (a). As seen before, the pattern of strongly increasing particle sizes with decreasing height evident in the volume radius (Fig. 4.5 (c)) is present here likewise. For the assumed geometrical shape, r_v and r_e do not coincide exactly, simply because they express different microphysical or rather optical properties of a crystal. Especially for a larger mean particle mass, both quantities differ to a certain extent (see Fig. 2.6). This is also found in comparing the cross sections of the two different radii. As pointed out before, the optical depth of the contrail cluster in Fig. 4.11 (b) is largest in in the level of major contrail

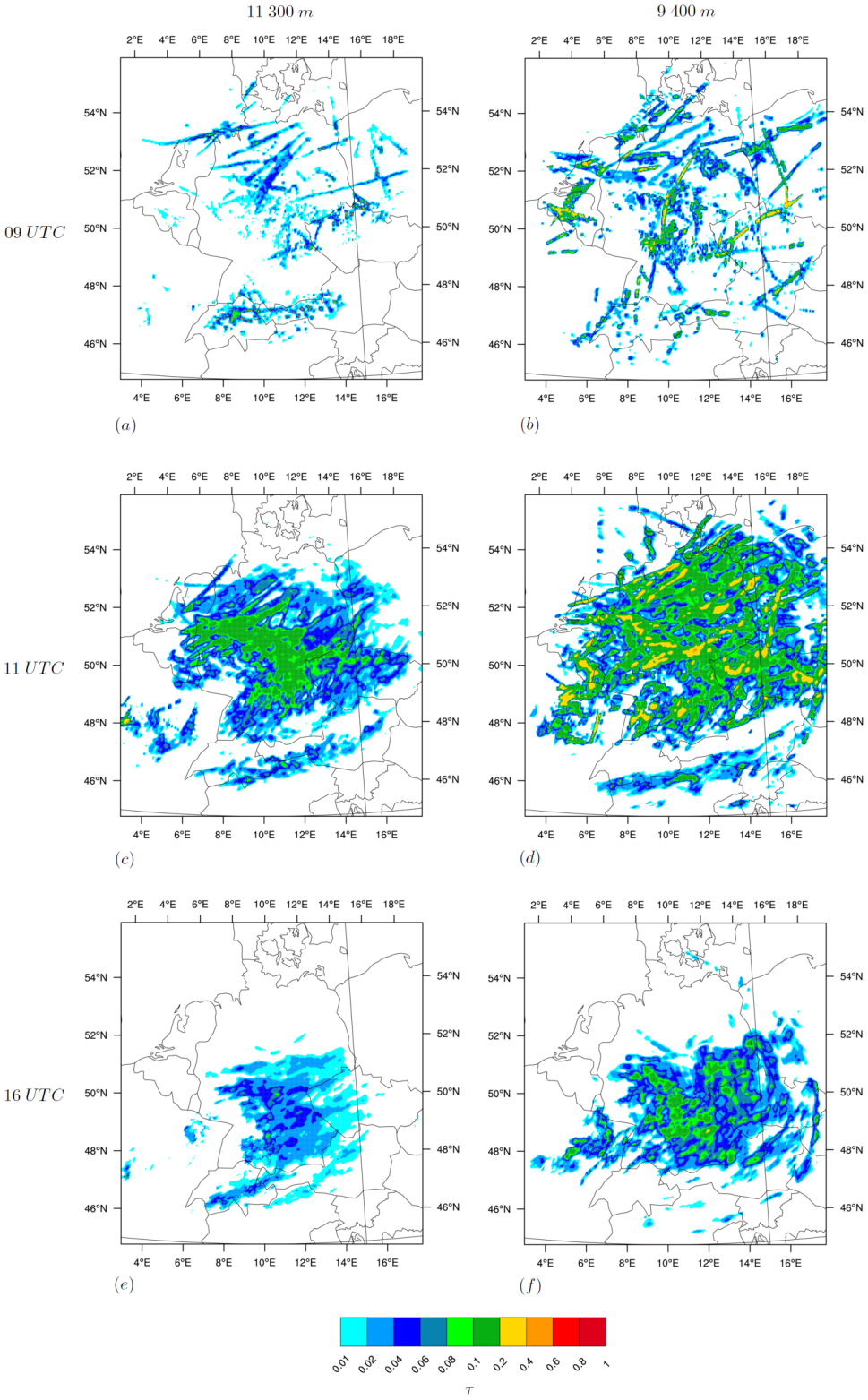

Figure 4.10: 3 December 2013: Contrail optical depth: 09 UTC (top), 11 UTC (center), 16 UTC (bottom); left column: 11 300 m, right column: 9 400 m.

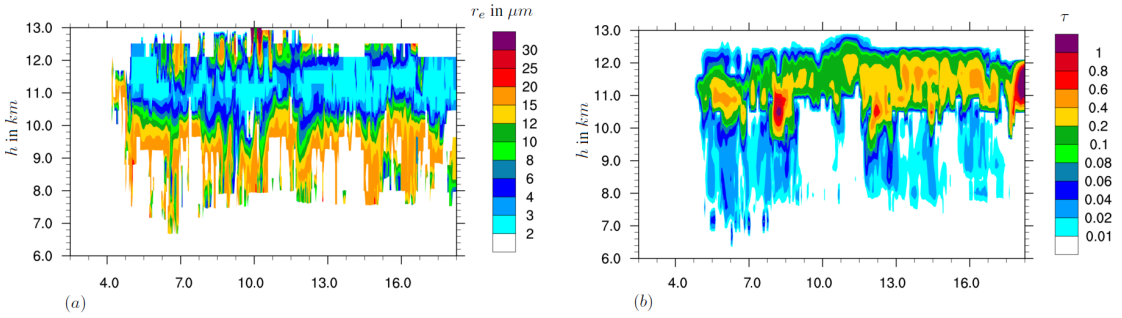

Figure 4.11: 3 December 2013, 12 UTC: Vertical cross section through contrail cluster: (a) particle effective radius, (b) optical depth.

forming, in heights between 12 km and 10 km.

4.4 Influence on the Radiative Budget

As the developed method is designed to be applied to predict energy yield of photovoltaic systems, especially the reduction of incoming solar radiation is of interest. But nevertheless, besides the latter, also the influence on thermal radiation as well as the total impact in terms of radiative forcing is presented.

The left column row of Fig. 4.12 shows the temporal evolution of contrails inhibiting solar radiation from reaching the earth's surface. Both direct as well as diffuse solar radiation are taken into account for this change in budget. As mentioned before, the first contrails are initialized at 08 UTC, therefore, the maximum age of contrails in Fig. 4.12 (a) is one hour. Obviously, additional ice particles contained in contrails reduce incoming solar energy. The young contrails have relatively low influence both spatially as well as in quantitatively. The spatial pattern finds itself in the pattern of inhibited solar radiation, as the majority of contrails are still narrow and not spread due to shear and sedimentation. Also, the very young and therefore small contrail ice particles with diameters and effective radii below the threshold of 2 μm are not taken into account in the radiation scheme. Probably, the impact here may be slightly underestimated. But nevertheless, single, young contrails reduce the incoming solar radiation in the order of magnitude of about 1 to 5 $W\ m^{-2}$, also seen the depiction of the sum of changes both in short- and longwave radiation (Fig. 4.13 (g)).

A strong increase of this effect is found at the second investigated temporal stage at 13 UTC (Fig. 4.12 (b)). Here, the contrail coverage reaches its maximum and also the resulting impact on short wave radiation is largest here. The most thick contrails, after Fig. 4.3 (b) located over central Germany and the eastern part of the domain, also produce a maximum cooling effect, reaching

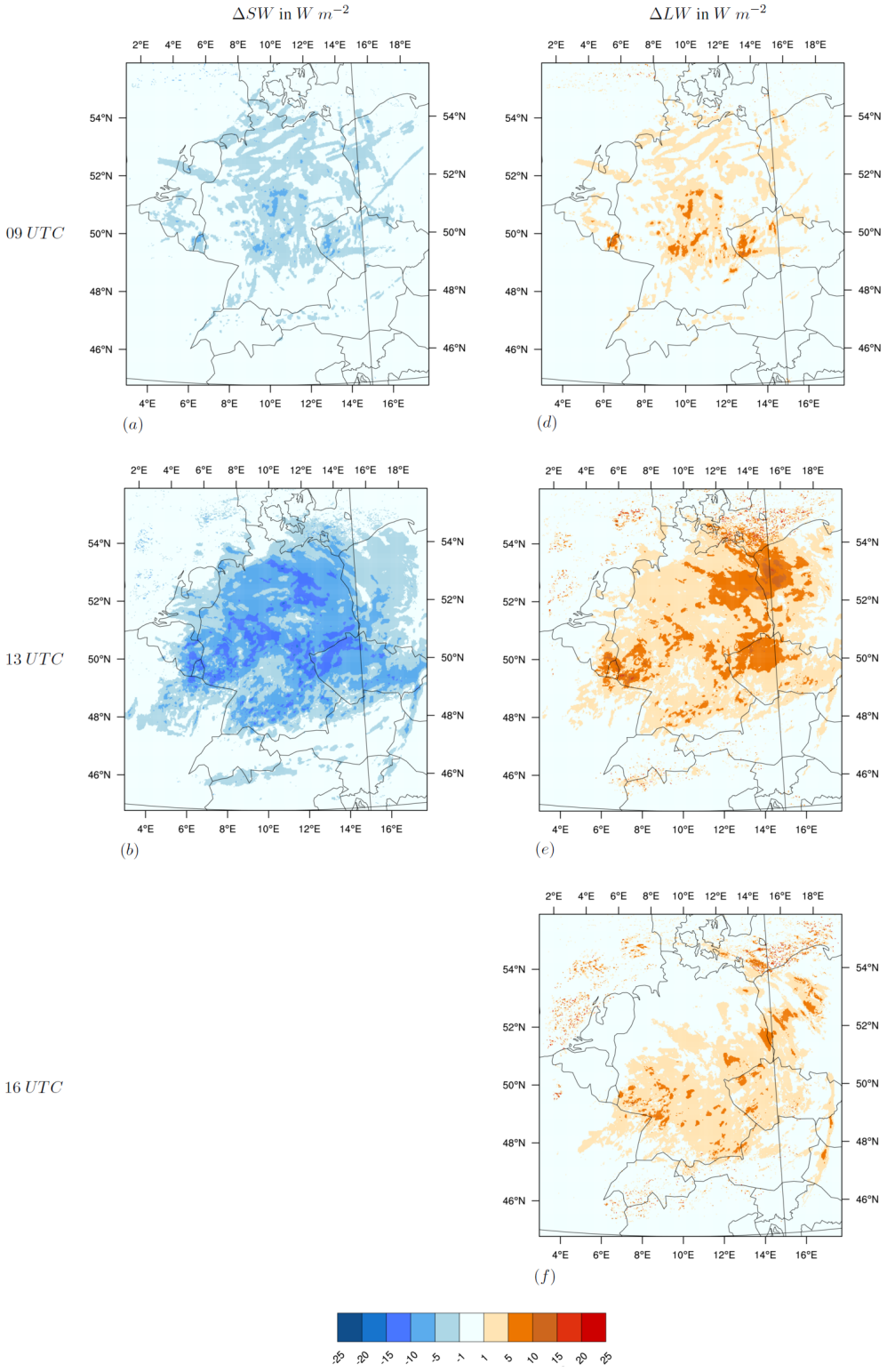

Figure 4.12: 3 December 2013, Influence of contrails on the radiative budget at the surface: loss of incoming short wave radiation (left), gain of absorbed thermal longwave radiation (right); top: 09 UTC, center: 13 UTC, bottom: 16 UTC.

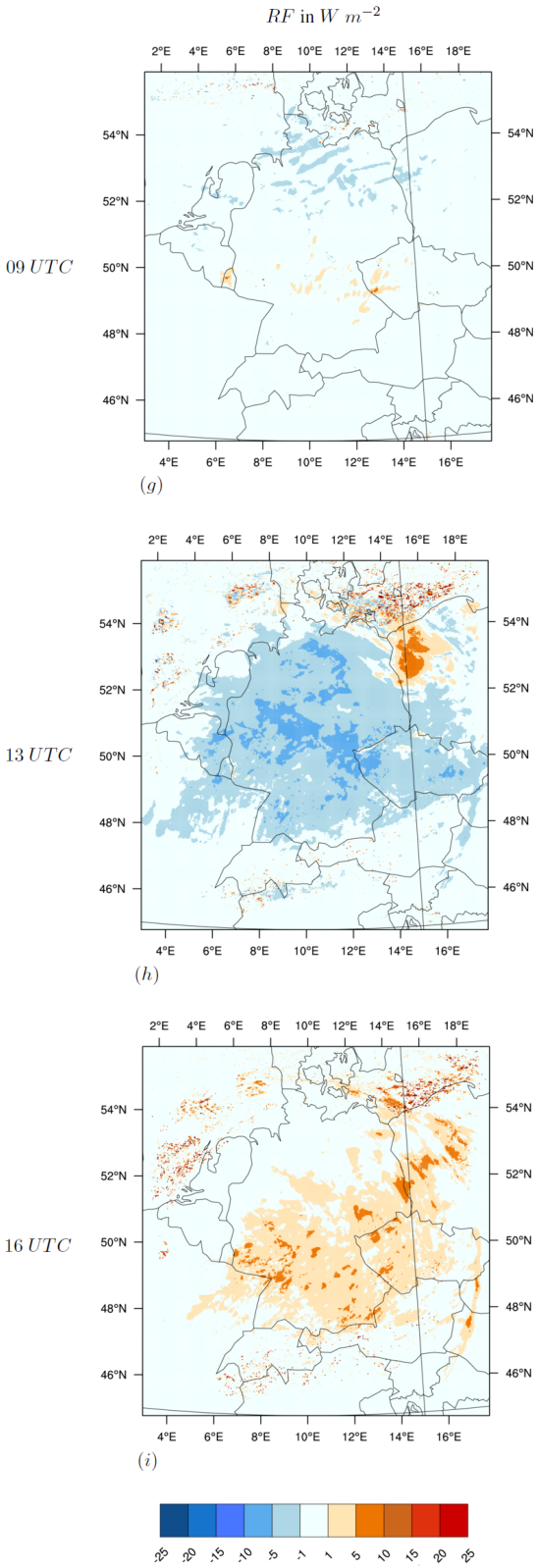

Figure 4.13: 3 December 2013, Influence of contrails on the radiative budget at the surface: total radiative budget; top: 09 UTC, center: 13 UTC, bottom: 16 UTC.

values up to $-15\ W\ m^{-2}$. This shading effect of contrails is of certain relevance for the production of solar energy. As the presented case study takes place at the beginning of December, days are rather short, so no impact on solar radiation is observed in the later part of the day.

Contrails and natural clouds likewise, have besides a cooling, also a warming effect, causing them to play an important role in anthropogenic impact on climate. The warming by reflecting thermal energy radiated from the surface and the atmosphere underneath the contrail and contrail cirrus cloud base is depicted in the right column of Fig. 4.12. The spatial pattern here is the same like for the short wave radiation, whereas certain differences in the intensity of the warming effect are present. As the surface temperatures are low in winter, also the warming effect of backscattering is relatively small and even at noon, does not exceed 5 to $10\ W\ m^{-2}$. After sunset, represented by Fig. 4.12 (f) and Fig. 4.13 (i), the effect is even stronger reduced, partly owing to the decreasing optical depth (Fig. 4.10 (e), (f)), partly caused by decreasing surface temperatures.

4.4.1 Impact on Photovoltaic Systems

Photovoltaic systems convert solar shortwave radiation into electrical energy. As presented above, contrails and contrail cirrus influence the amount of incoming shortwave radiation at the earth's surface and therefore modify the gain of such systems. The averaged loss of incoming direct and diffuse solar radiation for the 3 December 2013 is displayed in Fig. 4.14. The large and persistent contrail cluster over the Northern and Eastern part of the domain causes an average reduction of 5 to $30\ \%$ during approximately eight hours of daylight. At some locations in Northern Germany, reductions up to $40\ \%$ are calculated. The thin vail of contrail cirrus that spreads basically over the entire domain as seen in Fig. 4.3 (b) causes an averaged decrease of incoming direct and diffuse radiation in the order of 1 to $10\ \%$. The formerly mentioned slight drying effect due to contrails (4.7) results in an increase of the received amount of solar radiation of 1 to $5\ \%$, mainly over the North Sea.

Finally, the actual impact on photovoltaic systems is investigated. Fig. 4.15 (a) shows the temporal evolution of the total incoming shortwave radiation at a spot in the north-eastern part of the simulated domain, indicated by the red circle in Fig. 4.14. In this area, the loss of incoming shortwave radiation is the largest during the day. At $11\ UTC$, contrails and contrail cirrus reduce up to $80\ W\ m^{-2}$ of the incoming radiative power. Separating the total shortwave radiation in direct (Fig. 4.15 (b)) and diffuse (Fig. 4.15 (b)), it is obvious, that both quantities decrease when considering contrails in the model. As the additional cloud coverage influences the radiative budged besides of a negative impact considering the incoming direct radiation also by reflecting a certain fraction of incoming radiation, in the afternoon, a slight increase of diffuse radiation reaching ground is observed.

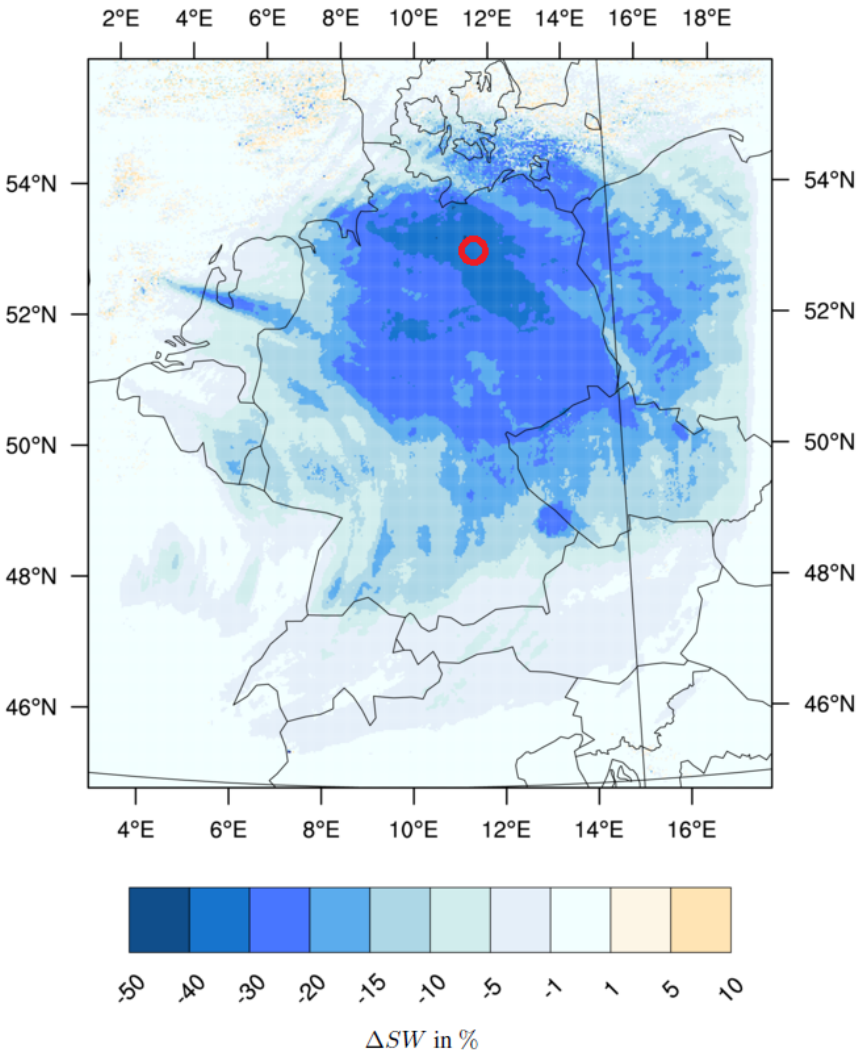

Figure 4.14: 3 December 2013: Averaged changes the amount of incoming diffuse and direct solar radiation at the surface.

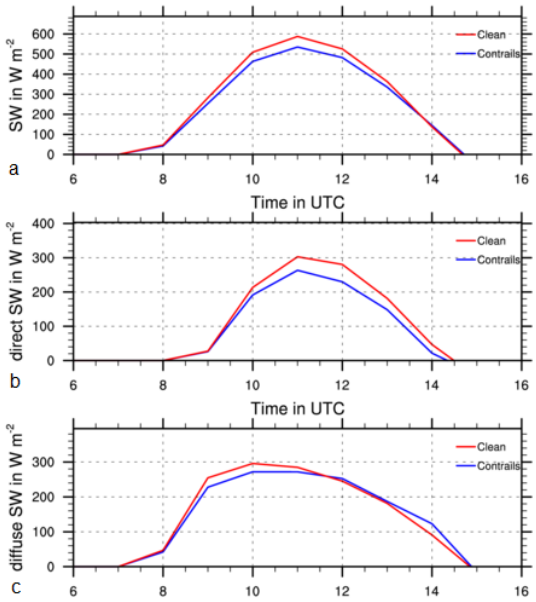

Figure 4.15: 3 December 2013: Temporal evolution incoming shortwave radiation with (blue) and without contrails (red): (a) total, (b) direct, (c) diffuse.

The overall picture indicates that contrails and contrail cirrus have a negative impact on the amount of produced photovoltaic power. Although the situation was chosen because of the relative high density of contrails, the effect is not negligible as usual weather forecasts, that do not consider aircraft induced cloudiness miss the reduction of up to 80 $W\ m^{-2}$ of received energy during one day.

4.4.2 Radiative Forcing

To estimate radiative forcing of a species, the difference in the radiative budget caused by this species between the received solar radiation at the top of the atmosphere and radiation reflected back into space is determined. The level to calculate the budget usually is defined to be the tropopause. Of course, one single day is not enough for naming the effect important for climate change, but still the developed method is applicable also for climate models.

For reasons of consistence, the same points in times like above are presented in Fig. 4.13. In agreement with the discussed modifications both in solar and thermal budget, a similar behavior is observed for the radiative forcing. During daytime, contrails cool the atmosphere by inhibiting solar energy from reaching the lower levels. Therefore, the overall radiative budget at 09 UTC (Fig. 4.13 (g)) is slightly negative. At 13 UTC (Fig. 4.13 (h)), a stronger impact up to $-5\ W\ m^2$ over distinct locations is present. During night, no cooling effect is possible due to the lack of solar radiation. Here (Fig. 4.13 (i)), contrails and contrail cirrus slightly warm the atmosphere in an order of magnitude below 5 $W\ m^{-2}$.

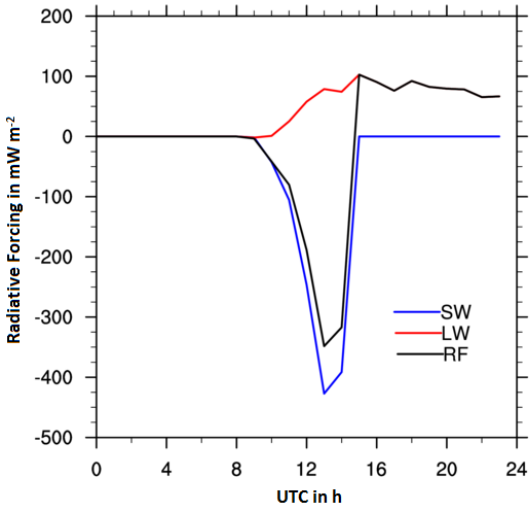

Figure 4.16: 3 December 2013, Temporal development of changes due to contrails and contrail cirrus in longwave (red), shortwave (blue) and total radiative forcing (black), averaged over 24 hours and the whole domain.

For comparing the results with studies using a coarser grid spacing, the total radiative budget was averaged over the entire domain and so representing the mean over an area of $15° \times 15°$. The temporal evolution of this quantity is depicted in Fig. 4.16. As seen before, during daytime, the cooling by reducing incoming short wave radiation, indicated by the blue line, is the major effect. The overall effect is reduced slightly by long wave warming, depicted by the red color. At night, no cooling effect takes place, the changes in radiative budget is only determined by the thermal warming. A $24-$hour-mean of the presented quantities yields for the short wave forcing $-50\ mW\ m^{-2}$, for the thermal wavelengths $40\ mW\ m^{-2}$ and for the overall effect $-10\ mW\ m^{-2}$ for the selected day. Here, the simulation does not agree with global model studies, that calculate spatially and temporal averaged radiative forcing from contrails and contrail cirrus of about 10 to $300\ mW\ m^{-2}$ over Europe (Burkhardt et al., 2011). Although the shortwave forcing agrees with these studies, the longwave budget does not. Main reason for this deviation is besides the short time to average especially the time of year. In winter, when days are short and surface temperatures low, the longwave impact is considerably smaller than in summer. Also the selected situation for this case study is not a usual one with contrails representing basically the entire high level cloud coverage over the domain.

But still the discussion of contrails impacting the radiative budget of the atmosphere enlightens an interesting issue. The effect is not easy to interpret, as for cases with contrails and natural cirrus competing for water vapor, the situation may be entirely different. Water vapor that is contained in contrail and contrail cirrus ice particles simply is not available to formation and deposition in

natural cirrus. This in turn changes the optical properties of high level cloud coverage in two ways. First, additional contrails and contrail cirrus occur, and second, the optical properties of natural clouds, they may even be replaced or at least delayed with respect to their onset by the first. Especially reduction of natural cirrus may offset the direct impact of contrails on radiation to a certain extent (Burkhardt et al., 2011).

5. Summary and Conclusions

In this study, the regional atmospheric model COSMO-ART, coupled with a two-moment scheme for microphysics and a diagnostic treatment of radiation, was extended by a parameterization for describing contrails.

The basic issue was to develop and implement a parameterization that decides whether the environmental conditions are favorable for the evolution of contrails and considers the characteristics of contrail formations by prescribing source terms for both ice mass and particle number concentrations of initial contrail ice crystals. The formation of contrails strongly depends on processes occurring in the wake vortex of the aircraft and underlies completely different nucleation regimes compared to natural ice clouds. Here, in virtue of the homogeneous nucleation caused by medium high supersaturation and a very high number of available condensation nuclei, initial ice particles are produced with diameters of about $1\ \mu m$. The corresponding initial particle number density in a young contrail crucially influences the microphysical and subsequently also the radiative contrail properties. Sensitivity studies helped to determine the fraction of the total initial crystal loss during the parameterized vortex stage.

In a next step, methods for a separate treatment of contrail ice were implemented to satisfy the special requirements occurring alongside of describing the microphysics in young contrails and the transition phase to contrail cirrus. It turned out, that initial contrail ice crystals are best described assuming hexagonal columns with small initial diameters. The most important processes here are depositional growth and sublimation. In a later state, also sedimentation and collection processes play an important role in contrail microphysics. It was shown, how microphysical properties such as ice water content, particle number density and the mean particle radius of crystal ensembles in a contrail change over time and reacting on the meteorological conditions. Young contrails content ice mass comparable to thin cirrus with 0.3 to $3.0\ mg\ m^{-3}$, whereas the latter is distributed on a huge particle number with densities up to $100\ cm^{-3}$ and radii below $5\ \mu m$. In the later stage of contrail cirrus, the mass remains merely constant, while the mean crystal diameter grows in an extent comparable to natural ice present in cirrus.

As the cloud microphysics scheme is online coupled to the model, feedback mechanism between contrails and the surrounding cirrus as well as the total amount of available water vapor could be

examined. Here, contrail cirrus tend to replace natural cirrus to a remarkable extent and cause changes in the microphysical appearance of high level cloud coverage, that in turn influences the radiative effect in these regions. Comparing the model results with satellite images for the same time revealed a good agreement, whereas the reference model run fell short in explaining the occurrence of several areas of high level cloudiness as they are mostly of artificial origin, appearing when the formation of contrails and contrail cirrus was allowed. Also, in-situ measurement and model lay in the same order of magnitude considering the microphysical and optical properties of the probed contrail.

In addition to the microphysical characteristics, also the radiative impact of contrails was investigated. Apparently, the used standard diagnostic radiation scheme had certain convergence issues with treating particles with small diameters like they are present in recently formed contrails. Partly due to the limited amount of time and partly as the error is rather minor, the very bottom end of the particle size distribution was neglected and only particles with diameters larger than $4\ \mu m$ were used in the radiation parameterization. Nevertheless, the evolution of changing optical properties in line with the transition of line shaped contrails to contrail cirrus und the formation of contrail induced cloudiness could be investigated. Young and line shaped contrails with small mean particle diameters do not influence the radiative budget of the atmosphere in a significant manner, in contrast, aged contrails and especially contrail cirrus does. The optical depth of contrails was found to be between 0.01 and 0.04 in young contrails and in contrast to other studies (Unterstrasser et al., 2010), reaching values up to 0.6 during the transition stage.

The developed method allowed investigating the impact of contrails and contrail cirrus on the radiative budget of the atmosphere, focusing on the impact of received shortwave solar radiation at the surface. Although the case study took place in December, when solar angles are low and the length of days is short, still a strong influence of contrails is observed, as they inhibit up to $15\ W\ m^{-2}$ of shortwave radiation from reaching the ground at noon. Considering the fact, that contrails are not taken into account in regional weather forecast, reduction of shortwave radiation to this extent may cause certain not predicted losses for photovoltaic systems.

This project was a first approach to simulate contrails on the high spatial and temporal resolution. Subsequently, the presented method can serve as a base to improve the predictability of the solar radiation budget in regional weather forecast by taking into account aircraft induced cloudiness. Also, due to the sophisticated microphysical basis without various usual simplifications, implementing the parameterization into a global model, the impact of contrails on natural cirrus and the radiative budget can be investigated on the global and climate relevant scale.

Bibliography

Appleman, H. (1953), The formation of exhaust condensation trails by jet aircraft, *Bull. Am. Meteorol. Soc.*, **34(1)** , 14 - 20.

Bakan, S., M. Betancor, V. Gayler and H. Grassl (1994), Contrail frequency over Europe from NOAA satellite images, *Ann. Geophys.* , **12**, 962 - 968.

Baldauf, M., A. Seifert, J. Forstner, D. Majewski, M. Raschendorfer and T. Reinhardt (2011) Operational convective-scale numerical weather prediction with the COSMO model: description and sensitivities, *Mon. Weather Rev.*, **139**, 3887 - 3905.

Böhm, H. P (1989), A general equation for the terminal fall speed of solid hydrometeors *J. Atmos. Sci.*, **46**, 2419 - 2427.

Burkhardt, U. and B. Kärcher (2009), Process-based simulation of contrail cirrus in a global climate model, *J. Geophys. Res.*, **114** , D16201.

Burkhardt, U. and B. Kärcher (2011), Global radiative forcing from contrail cirrus, *Nat. Clim. Change*, **1(1)** , 54 - 58.

Burkhardt, U., B. Kärcher, M. Ponater, K. Gierens and A. Gettelman (2005), Contrail cirrus supporting areas in model and observations, *Geophys. Res. Lett.*, **35**, L16808.

Burkhardt, U., B. Kärcher and U. Schumann (2010), Global Modeling of the Contrail and Contrail Cirrus Climate Impact, *Bull. Amer. Meteor. Soc.*, **91**, 479 - 484.

Doms, G., J. Förstner, E. Heise, H.-J. Herzog, D. Mironov, M. Raschendorfer, T. Reinhardt, B. Ritter, R. Schrodin, J.-P. Schulz and G. Vogel (2011), A description of the nonhydrostatic regional cosmo model.

EASA, 2015, http://easa.europa.eu/document-library/icao-aircraft-engine-emissions-databank, 30.06.2015.

Ebert, E. and J. Curry (1992), A parameterization of ice cloud optical properties for climate models, *J. Geophys. Res. Atmos.*, **97(D4)**, 3831 - 3836.

Eleftheratos, K., C. Zerefos, P. Zanis, D. Balis, G. Tselioudis, K. Gierens, and R. Sausen (2007), A study on natural and manmade global interannual fluctuations of cirrus cloud cover for the period 1984-2004, *Atmos. Chem. Phys.*, **7** , 2631 - 2642.

Febvre, G., J. - F. Gayet, A. Minikin, H. Schlager, V. Shcherbakov, O. Jourdan, R. Busen, M. Fiebig, B. Kärcher and U. Schumann (2009), On optical and microphysical characteristics of contrails and cirrus, *J. Geophys. Res.*, **114**, D02204.

Ferrone, A. (2011), Aviation and climate change in Europe: from regional climate modelling to policy-options, Prom. : van Ypersele, J. - P.

flightradar24.com, (2015), http://www.flightradar24.com, 16.08.2015.

Forster, P., V. Ramaswamy, P. Artaxo, et al. (2007), Changes in atmospheric constituents and in radiative forcing, Climate Change 2007 The Physical Science Basis, Contribution of Working Group I to the Fourth Assessment Report of the IPCC. Climate Change 2007 The Physical Science Basis, Contribution of Working Group I to the Fourth Assessment Report of the IPCC edited by: Solomon, S., Quin, D., Manning, M., et al., *Cambridge University Press, Cambridge, United Kingdom and New York, NY, USA*, 129 - 234.

Fu, Q., P. Yang and W.B. Sun (1998), An Accurate Parameterization of the Infrared Radiative Properties of Cirrus Clouds for Climate Models, *J. Clim.*, **11**, 2223 - 2237.

Gierens, K (1996), Numerical simulations of persistent contrails, *J. Atmos. Sci.*, **53**, 3333 - 3348.

Gierens, K., U. Schumann , H. G. J. Smit, M. Helten and G. Zängl (1997), Determination of humidity and temperature fluctuations based on MOZAIC data and parametrisation of persistent contrail coverage for general circulation models, *Ann. Geophys.*, **15**, 1057 - 1066.

Hall, W. D. and H. R. Pruppacher (1976) The survival of ice particles falling from cirrus clouds in subsaturated air, *J. Atmos. Sci.* , **33**, 1995 - 2006.

Harrington, J., M. Meyers, R. Walko and W. Cotton (1995), Parameterization of ice crystals conversion processes due to vapor deposition for mesoscale models using doublemoment basis functions. I - Basic formulation and parcel model results, *J. Atm. Sci.*, **52(23)**, 4344 - 4366.

Hendricks, J., B. Kärcher, U. Lohmann, and M. Ponater (2005), Do aircraft black carbon emissions affect cirrus clouds on the global scale, *Geophys. Res. Lett.*, **32**.

Heymsfield, A., D. Baumgardner, P. DeMott, P. Forster, K. Gierens, and B. Kärcher (2010), Contrail Microphysics, *Bull. Amer. Meteor. Soc.*, **91**, 465 - 472.

Holzäpfel, F. and T. Gerz (1999), Two-dimensional wake vortex physics in the stably stratified atmosphere, *Aeros. Sci. Techn.*, **5**, 261 - 270.

Jensen, E. J., O. B. Toon, R. F. Puesche, J. Goodman, G. W. Sachse, B. E. Anderson, K. R. Chan, D. Baumgardner, R. C. Miake-Ly (1998), Ice crystal nucleation and growth in contrails forming at low ambient temperatures, *Geophys. Res. Lett.*, **25**, 1371 - 1374.

Jensen, E. J., O. B. Toon, S. Kinne, G. W. Sachse, B. E.Anderson, K. R. Chan, C. H. Twohys, B. Gandruds, A. Heymsfields and R. C. Miake-Ly (1998), Environmental conditions required for contrail formation and persistence, *J. Geophys. Res.*, **103**, 3929 - 3936.

Kärcher, B. and S. Solomon (1999), On the composition and optical extinction of particles in the tropopause region, *J. Geophys. Res.*, **104** , 27,441 - 27,459.

Kärcher, B. and U. Lohmann (2002), A parameterization of cirrus cloud formation: Homogeneous freezing of supercooled aerosols, *J. Geophys. Res.*, **107**, 4010.

Kärcher, B. and U. Lohmann (2003), A parameterization of cirrus cloud formation: Heterogeneous freezing, *J. Geophys. Res.*, **108**, 4402.

Kärcher, B. (2002), Properties of subvisible cirrus clouds formed by homogeneous freezing, *Atmos. Chem. Phys.*, **2**, 161 - 170.

Kärcher B., O. Möhler, P. J. DeMott, S. Pechtl and F. Yu (2007), Insights into the role of soot aerosols in cirrus cloud formation, *Atmos. Chem. Phys.*, **7**, 4203 - 4227.

Key, J. R., P. Yang, B. A. Baum and S. L. Nasiri (2002), Parameterization of shortwave ice cloud optical properties for various particle habits, *J. Geophys. Res.*, **107**, AAC 7.1 - AAC 7.10.

Köhler, C. and A. Seifert, (2015), Identifying sensitivities for cirrus modelling using a two-moment two-mode bulk microphysics scheme, *Tellus B*, **67**, 24494.

Koop, T., B. Luo, A. Tsias and T. Peter (2000), Water activity as the determinant for homogeneous ice nucleation in aqueous solutions, *Nature*, **406** , 611 - 614.

Lawson, R. P., A. J. Heymsfield, S. M. Aulenbach and T. L. Jensen (1998), Shapes, sizes and light scattering properties of ice crystals in cirrus and a persistent contrail during SUCCESS, *Geophys. Res. Lett.* , **25**, 1331-1334.

Lewellen, D., and W. Lewellen (2001), The effects of aircraft wake dynamics on contrail development, *J. Atmos. Sci.*, **58(4)**, 390 - 406.

Mannstein, H., R. Meyer, and P. Wendling (1999), Operational detection of contrails from NOAA-AVHRR-data, *Int. J. Remote Sensing*, **20(8)**, 1641 - 1660.

Mannstein, H. and U. Schumann (2005), Aircraft induced contrail cirrus over Europe, *Meteorol. Z.*, **14**, 549 - 554.

Marquart, S., M. Ponater, F. Mager, and R. Sausen (2003), Future development of contrail cover, optical depth and radiative forcing: Impacts of increasing air traffic and climate change, *J. Clim.*, **16(17)**, 2890 - 2904.

Meerkötter, R., U. Schumann, D. R. Doelling, P. Minnis, T. Nakajima and Y. Tsushima (1998), Radiative forcing by contrails, *Ann. Geophys.*, **17**, 1080 - 1094.

Meyer, R., H. Mannstein, R. Meerkötter, U. Schumann, and P. Wendling (2002), Regional radiative forcing by line-shaped contrails derived from satellite data, *J. Geophys. Res. Atmos.*, **107(10.1029)**.

Minnis, P., S. T. Bedka, D. P. Duda, K. M. Bedka, T. Chee, J. K. Ayers, R. Palikonda, D. A. Spangenberg, K. V. Khlopenkov and R. Boeke (2013), Linear contrail and contrail cirrus properties determined from satellite data, *Geophys. Res. Lett.*, **40**, 3220 - 3226.

Minnis, P., R. Palikonda, B. J. Walter, J. K. Ayers, and H. Mannstein (2005), Contrail properties over the eastern north pacific from avhrr data, *Meteorol. Z.*, **14**, 515 - 523.

Minnis, P., U. Schumann, D. R. Doelling, K. Gierens and D. W. Fahey (1999), Global distribution of contrail radiative forcing, *Geophys. Res. Lett.*, **26** , 1853 - 1856.

ML-CIRRUS, (2014), http://www.pa.op.dlr.de/ML-CIRRUS/index.html, 16.08.2015.

Myhre, G., D. Shindell, F.-M. Bréon, W. Collins, J. Fuglestvedt, J. Huang, D. Koch, J.-F. Lamarque, D. Lee, B. Mendoza, T. Nakajima, A. Robock, G. Stephens, T. Takemura and H. Zhang (2013), Anthropogenic and Natural Radiative Forcing. In: Climate Change 2013: The Physical Science Basis. Contribution of Working Group I to the Fifth Assessment Report of the Intergovernmental Panel on Climate Change [Stocker, T.F., D. Qin, G.-K. Plattner, M. Tignor, S.K. Allen, J. Boschung, A. Nauels, Y. Xia, V. Bex and P.M. Midgley (eds.)], *Cambridge University Press, Cambridge, United Kingdom and New York, NY, USA.*

Palikonda, R., P. Minnis, D. P. Duda, and H. Mannstein (2005), Contrail coverage derived from 2001 avhrr data over the continental united states of america and surrounding areas, *Meteorol. Z.*, **14**, 525 - 536.

Ponater, M., S. Brinkop, R. Sausen, and U. Schumann (1996), Simulating the global atmospheric response to aircraft water vapour emissions and contrails: a first approach using a GCM, *Ann. Geophys.*, **14(9)**, 941 - 960.

Ponater, M., S.Marquart, and R. Sausen (2002), Contrails in a comprehensive global climate model: Parameterization and radiative forcing results, *J. Geophys. Res. Atmos.*, **107(13)**, 941 - 960.

Ponater, M., S. Marquart, R. Sausen, and U. Schumann (2005), On contrail cimate sensitivity, *Geophys. Res. Lett.*, **32**, L10706-1 - L10706-5.

Pruppacher H. R. and J. D. Klett JD (1997), Microphysics of clouds and precipitation. *Dordrecht: Kluwer Academic Publishers* .

Ritter, B. and J. F. Geleyn (1992), A comprehensive radiation scheme for numerical weather prediction models with potential applications in climate simulations, *Mon. Weather Rev.,* , **120 (2)**, 303 - 325.

Sausen, R., I. Isaksen, V. Grewe, D. Hauglustaine, D. Lee, G. Myhre, M. Köhler, G. Pitari, U. Schumann, F. Stordal, et al. (2005), Aviation radiative forcing in 2000: An update on IPCC (1999), *Meteorol. Z.*, **14(4)**, 555 - 561.

Schmidt, E. (1941), Die Entstehung von Eisnebel aus den Auspuffgasen von Flugmotoren, *Schriften der Deutschen Akademie der Luftfahrtforschung*, **44**, 1 - 15.

Schumann, U. (1996), On conditions for contrail formation from aircraft exhausts, *Meteorol. Z.*, **NF 5**, 4 - 23.

Schumann, U. (2005), Formation, properties and climatic effects of contrails, *C. R. Physique*, **6**, 549 - 565.

Schumann, U. (2012), A contrail cirrus prediction model, *Geosci. Model Dev.*, **5**, 543 - 580.

Schumann, U. and K. Graf (2013), Aviation-induced cirrus and radiation changes at diurnal timescales, *J. Geophys. Res.*, **118**, 2404 - 2421.

Schumann, U. J. E. Penner, Y. Chen, C. Zhou and K. Graf (2015), Dehydration effects from contrails in a coupled contrail-climate model, *Atmos. Chem. Phys.* , , in press.

Schumann, U., H. Schlager, F. Arnold, R. Baumann, P. Haschbergera and O. Klemm (1998), Dilution of aircraft exhaust plumes at cruise altitudes, *Atmos. Environ.*, **32**, 3097 - 3103.

Schröder, F., B. Kärcher, C. Duroure, J. Ström, A. Petzold, J.- F. Gayet, B. Strauss, P. Wendling and S. Borrmann (2000), On the Transition of Contrails into Cirrus Clouds, *J. Atm. Sci.*, **57,** , 464 - 480.

Seifert, A. and K. D. Beheng (2006), A two-moment cloud microphysics parameterization for mixed-phase clouds. part 1: Model description, *Meteorol. Atmos. Phys.*, **92**, 45 - 66.

Spichtinger, P. and K. Gierens (2009), Modelling of cirrus clouds - Part 1a: Model description and validation, *Atmos. Chem. Phys.*, **9**, 685 - 706.

Stubenrauch, C. and U. Schumann (2005), Impact of air traffic on cirrus coverage, *Geophys. Res. Lett.*, **32**.

Sussmann, R. and K. Gierens (2009), Lidar and numerical studies on the different evolution of vortex pair and secondary wake in young contrails, *J. Geophys. Res.*, **104**, 2131 - 2142.

Unterstrasser, S. (2008), Numerische Simulationen von Kondensstreifen und deren Übergang in Zirren, Prom. : Schumann, U.

Unterstrasser, S. (2014), Large-eddy simulation study of contrail microphysics and geometry during the vortex phase and consequences on contrail-to-cirrus transition, *J. Geophys. Res. Atmos.*, **119**, 7537 - 7555.

Unterstrasser, S. (2016s), Properties of young contrails - A parametrisation based on numerical simulations, *Atmos. Chem. Phys., in press*.

Unterstrasser, S. and K. Gierens (2010), Numerical simulations of contrail-to-cirrus transition - Part 1: An extensive parametric study *Atmos. Chem. Phys.*, **10**, 2017 - 2036.

Vázquez-Navarro, M, B. Mayer and H. Mannstein (2012), A fast method for the retrieval of integrated longwave and shortwave top-of-atmosphere irradiances from MSG / SEVIRI (RRUMS), *Atmospheric Measurement Techniques Discussions.*, **5**, 4969 - 5008.

Vogel, B. H. Vogel, D. Bäumer, M. Bangert, K. Lundgren, R. Rinke and T. Stanelle (2009), The comprehensive model system COSMO-ART - Radiative impact of aerosol on the state of the atmosphere on the regional scale, *Atmos. Chem. Phys.*, **9**, 8661 - 8680.

Voigt, C., U. Schumann, T. Jurkat, D. Schäuble, H. Schlager, A. Petzold, J. - F. Gayet, M. Krämer, J. Schneider, S. Borrmann, J. Schmale, P. Jessberger, T. Hamburger, M. Lichtenstern, M. Scheibe, C. Gourbeyre, J. Meyer, M. Kübbeler, W. Frey, H. Kalesse, T. Butler, M. G. Lawrence,F. Holzäpfel, F. Arnold,M. Wendisch, A. Döpelheuer,K. Gottschaldt, R. Baumann, M. Zöger, I. Sölch, M. Rautenhaus, and A. Dörnbrack (2010), In-situ observations of young contrails - overview and selected results from the CONCERT campaign, *Atmos. Chem. Phys.*, **10**, 9039 - 9056.

Zängl, G., D. Reinert, P. Rípodas and M. Baldauf (2015) The ICON (ICOsahedral Non-hydrostatic) modelling framework of DWD and MPI-M: Description of the non-hydrostatic dynamical core, *Q. J. R. Meteorol. Soc.*, **141**, 563 - 579.

Zondag, H. A. (2008) Flat-plate PV-Thermal collectors and systems: A review, *Renew. Sustain. Energy Rev.* , **12(4)**, 891 - 959.

List of Figures

List of Tables

A. List of Symbols

Symbol	Definition
ad	adiabatical
c	contrails
$coll$	collection
d	dry air
dep	deposition
e	environment
i	ice
l	liquid water
$melt$	melting
p	plume
sat	saturation
sed	sedimentation
sub	sublimataion
v	water vapor or volume

Symbol	Definition	Unit
β	extiction coefficient	m^{-1}
Γ	gamma function	$-$
ΔI_v	loss of ice mass in aircraft wake	$kg\ kg^{-1}$
ϵ	M_v/M_l	$-$
η	effectiveness	$-$
λ	slope in size distribution	$kg^{-\mu}$
μ	constant in size distribution	$-$
ν	constant in size distribution	$-$
ν_x	kinematic viscosity of species x	$m^2\ s^{-1}$
ρ	density of air	$kg\ m^{-3}$
ρ_x	density of species x	$kg\ m^{-3}$
τ	optical thickness or time scale	$-$ or s

$\vec{\Omega}$	angular speed of Earth's rotation	s^{-1}
$\widetilde{\omega}$	single scattering albedo coefficient	$-$
a_{geo}	constant in diameter-mass-relation	$m^{-1}\ kg^{-b_{geo}}$
a_{vel}	constant in fallspeed relation coefficient	$m\ s^{-1}\ kg^{-b_{vel}}$
a_{ven}	constant in ventilation coefficient	$-$
b_{geo}	constant in diameter-mass-relation	$-$
b_{vel}	constant in fallspeed relation coefficient	$-$
b_{ven}	constant in ventilation coefficient	$-$
c_i	constant in capacity for ice	$-$
C_i	capacity of ice	$-$
c_p	specific heat capacity of air for $p = const$	$kg\ m^{-2}$
D	diameter	m
D_x	diffusivity of species x	m
e	partial pressure	hPa
E	collection efficiency	$-$
$e_{sat,x}$	saturation pressure for phase x	hPa
e_x	partial pressure for species x	hPa
EI_x	emission index for species x	$kg\ kg^{-1}$
f	transmission factor	$-$
F	thrust of the engine	N
f_m	loss factor in vortex parameterization	$-$
f_n	weighting factor in vortex parameterization	$-$
F_{ven}	Ventilation coefficient	$-$
f_x	number density size distribution for spezies x	$m^{-3}\ kg^{-1}$
$\vec{F}_x$	turbulent flux of species x	$kg\ m^{-2}\ m^{-1}$
g	asymmetry factor	$-$
$\vec{g}$	gravitational acceleration	$m\ s^{-2}$
G	slope of the mixing line between exhaust plume	PaK^{-1}
	and sourrounding air	$-$
h	specific enthalpy	$J\ kg^{-1}$
I_c	Initial contrail ice mass mixing ratio	$kg\ kg^{-1}$
I_x	sources / sinks of species x	$kg\ m^{-3}\ s^{-1}$
I_0	Contrail ice mass mixing ratio at stage 0	$kg\ kg^{-1}$
IWC	ice water content	$mg\ m^{-3}$
IWP	ice water path	$g\ m^{-2}$
K_h	turbulent diffusivity of heat	$m^2\ s{-}1$
K_T	conductivity of heat	$J\ m^{-1}\ s^{-1}\ K^{-1}$
K_{xy}	kernel for collecting spezies x and y	$m^3\ s^{-1}$
L	crystal width or mass density	m or $kg\ m^{-3}$

L_{xy}	latent heat of phase transistion x to y	$J\ kg{-}1$
$\dot{m}_f$	fuel flow	$kg\ s^{-1}$
M_x	molar mass of specis x	kg
M_x^n	moment to the power of n of spcies x	$kg^n\ m^{-3}$
N	number density	cm^{-1}
N_{BV}	Brunt-Vaisaila frequency	s^{-1}
N_{dil}	dilution factor	$-$
N_{Re}	Reynolds number	$-$
N_{Sc}	Schmid number	$-$
p	pressure	hPa
$\vec{P}_x$	precipitation	mmd^{-1}
Q	specific heat of combustion	$J\ kg^{-1}$
Q_h	diabatical heating / cooling	$Pa\ s^{-1}$
$q_{sat,x}$	specific saturation mixing ratio for phase x	$kg\ kg^{-1}$
q_x	specific mass mixing ratio for phase x	$kg\ kg^{-1}$
r_e	effective radius	μm
r_v	volume radius	μm
RH	relative humidity with respect to liquid water	$-$
RH_i	relative humidity with respect to ice	$-$
R_x	specific gas constant for species x	$J\ kg^{-1}\ K^{-1}$
S_i	supersaturation with respect to ice	$-$
t	time	s
T	temperature	K
T_f	temperature of exaust gases	K
T_{LC}	threshold temperature for the Schmidt-Appleman-	K
	Criterion	$-$
T_{LM}	maximum threshold temperature for the Schmidt-	K
	Appleman-Criterion	$-$
T_3	temperature of freezing point	K
$\mathbb{T}$	Reynolds Stress tensor	Pa
v	velocity	$m\ s^{-1}$
$\vec{v}$	wind velocity	$m\ s^{-1}$
w	vertical velocity	$m\ s^{-1}$
x	mass of single particle	kg
z	geometrical height	m

B. Fits for the Optical Properties

Table B.1: Fit coefficients for solar $RG92$ interval, used in Eqs. 2.39 - 2.43 (Fu et al., 1998)

	extinction in m^{-1}	coalbedo in m^{-1}	asymetry factor	forward scattered fraction
1.	$1.66211\ 10^{-4}$	$6.56635\ 10^{-2}$	$7.83650\ 10^{-1}$	$9.69848\ 10^{-2}$
2.	2.50326	$2.00282\ 10^{-3}$	$2.07418\ 10^{-3}$	$-2.59146\ 10^{-4}$
3.	$1.40601\ 10^{-3}$	$-1.13681\ 10^{-5}$	$-1.39186\ 10^{-5}$	$3.38488\ 10^{-6}$
4.	$-$	$3.48439\ 10^{-8}$	$3.96581\ 10^{-8}$	$-1.53793\ 10^{-8}$

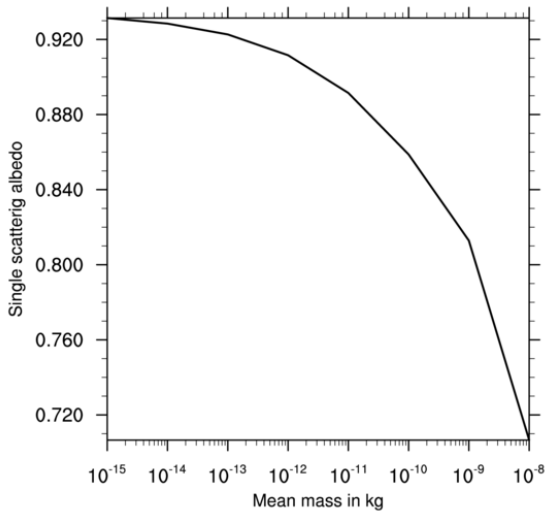

Figure B.1: Single scattering albedo (Eq. 2.40) for contrail ice particles.

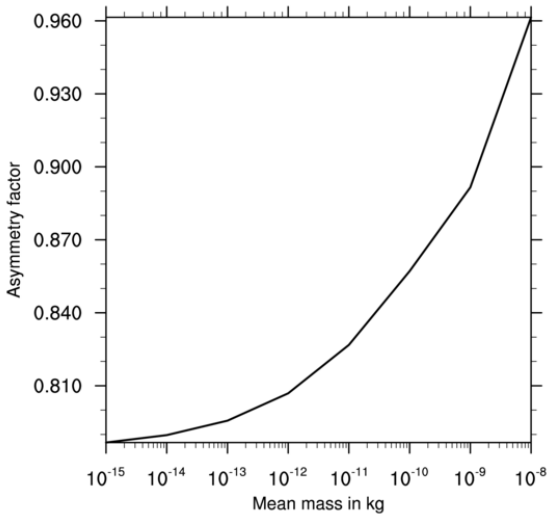

Figure B.2: Asymmetry factor (Eq. 2.41) for contrail ice particles.

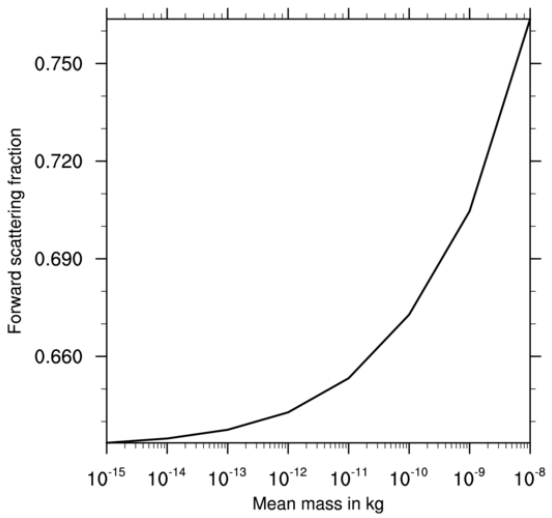

Figure B.3: Forward scattering fraction (Eq. 2.43) for contrail ice particles.

C. Parameters for Aircrafts and Fuel

Table C.1: Fuel parameters.

Fuel parameter	Unit	Value
Hydrogen mass fraction m_H	$kg\ kg^{-1}$	0.14
Specific combustion heat Q	$MJ\ kg^{-1}$	43.0
Emission index of water EI_{H_2O}	$kg\ kg^{-1}$	1.25
Emission index of CO_2 EI_{CO_2}	$kg\ kg^{-1}$	3.15
Emission index of BC EI_{soot}	kg^{-1}	10^{14}

Table C.2: Aircraft and engine parameters.

Parameter	Unit	large (B747)	medium (A330)	small (B737)
η	(1)	0.3	0.3	0.3
span s	m	64.4	60.0	34.4
mass M	Mg	310.0	190.0	65.0
v_0	$m\ s^{-1}$	250.0	240.0	230.0
F	kN	254	145.0	92.0
$\dot{m}_f$	$g\ s^{-1}$	2.28	1.31	0.93
EI_{soot}	kg^{-1}	10^{14}	10^{14}	10^{14}

D. Acknowledgment

Finally, it is time to say thank you to all that contributed to this project. I am very grateful to Prof. Dr. Christoph Kottmeier for supervising this thesis and also to Prof. Dr. Corinna Hoose for accepting to co-supervise me, her interest in this work and the helpful suggestions.

Best of all, i want to express my very deep gratitude to Bernhard Vogel, who encouraged me to begin this thesis, who continuously supported and motivated me with his new ideas and his great scientific curiosity. Also thank you for establishing various fruitful connections to the contrails-community. Next, i am very grateful to Heike Vogel, for encouraging me, for always having some time and energy left to give help and advice with many different issues and for continuously motivating me to abandon a bad attitude.

Also thanks a lot to my roommates Tobias Schad and Konrad Deetz for the nice working atmosphere and of course to all the other members of our working group. Valuable discussions concerning scientific and non-scientific topics, given hints and supported technical problems eased my life a lot.

Furthermore, i am very grateful to the colleagues from Cologne, Jan Bechtold, Martin Jung and Henry Pak who provided the tracks and answered all of my questions.

I am very grateful to Simon Unterstrasser, for being so interested in this project, for the fruitful discussions and advices, for kindly providing me with routines and especially for supporting me in Bad Kohlgrub.

Prof. Dr. Schumann also assured himself of my gratitude for his motivating interest. In this context, i would also like to deeply thank Prof. Dr. Robert Saussen, Lisa Bock, Ulrike Burkhardt, Klaus Gierens, Kaspar Graf and Margarita Vázquez-Navarro for warmly welcome me and kindly spending some time for me and my project, providing me with lots of new ideas and deeper insights in the topic.

An dieser Stelle ein ganz spezielles Dankeschön an die Jungs einer kleinen mittelständischen Gerüstbaufirma, die ihr zwar von meinem Studium wenig gehalten habt und wohl auch diese

Danksagung nie lesen werdet, mich aber all die Jahre bei der Stange und auf dem Boden gehalten habt und immer da wart, wenn Not am Mann war.

Finally, thanks to all those friends and co-students for having such a nice time alongside studying. Thanks to my family for supporting me during all the years, and without whom this Master's degree would not have been possible.

And some very special thank-you to Pila, it is nice, you are there.

Erklärung

Hiermit erkläre ich, dass ich die vorliegende Arbeit selbst verfasst und nur die angegebenen Hilfsmittel verwendet habe.

Ich bin damit einverstanden, dass diese Arbeit in Bibliotheken eingestellt wird und vervielfältigt werden darf.

Karlsruhe, den 6. Oktober 2015

Simon Gruber